Advanced Circuit Configurations for RF Wireless Power Transfer

Zhanel Kudaibergenova

Submitted in fulfillment of the requirements for the degree of Master of Science in Electrical and Computer Engineering

School of Engineering and Digital Sciences Department of Electrical and Computer Engineering Nazarbayev University

53 Kabanbay Batyr Avenue, Astana, Kazakhstan, 010000

Supervisor: Mohammad Hashmi

Co-supervisor: Carlo Molardi

26 April 2024

Table of Contents

Abstract

Technology for wireless power transfer (WPT) has gained more importance in the contemporary world. The upsurge spike can be a result of the WPT system's ability to power devices without the use of traditional connections. In particular, near-field WPTs have a wide range of applications, including wireless sensors, IoT, biomedical implants, RFID, and consumer electronics. It is essential to emphasize that the WPT system can be realized in a number of ways,

one of which is a defected ground structure technique. This approach is well-established for its simple design process and compact system. Despite this recently developed DGS-based WPTs demonstrate poor performance, in other words, low power transfer efficiency in practical validations. The inevitable factors, such as imperfections of lumped elements, the in-house fabrication, and energy losses during transfer, have an impact on the experimental results. Therefore, various performance enhancement strategies have to be considered to realize the compact and efficient WPT system. In this regard, one of the promising methods for improving WPT operation is the use of metamaterial, which is an artificial material with unique electromagnetic features. As a result, this thesis work focuses on the development of compact and efficient WPTs applicable to various fields and on performance enhancement strategies based on metamaterial utilization.

List of Abbreviations

ADS Advanced Design System

CPT Capacitive power transfer

CST Computer Simulation Technology

DGS Defected ground structure

DNG Double negative

EC Equivalent circuit

EM Electromagnetic

FoM Figure of Merit

IoT Internet of things

IPT Inductive power transfer

ML Microstrip line

MRC Magnetic resonant coupling

MTM Metamaterial

PTE Power transfer efficiency

RFID Radio Frequency Identification

Rx Receiver

SAR Specific absorption rate

SRR Split-ring resonator

Tx Transmitter

UAV Unmanned aerial vehicle

WPT Wireless power transmission

List of Publications

Z. Kudaibergenova and M. Hashmi, "Experimental Performance Evaluation of Compact WPT System for Biomedical Applications," *2023 Asia-Pacific Microwave Conference (APMC)*, Taipei, Taiwan, 2023, pp. 447-449.

Z. Kudaibergenova, K. Dautov, and M. Hashmi, "Evaluation of Bending Effect on the DGS-based WPT System Efficiency," *2024 IEEE International Symposium on Antennas and Propagation and ITNC-USNC-URSI Radio Science Meeting*, Florence, Italy, 2024, pp. 1-2. (Accepted for publication)

Z. Kudaibergenova, K. Dautov, G. Nauryzbayev, and M. Hashmi, "Effective Use of Metamaterial Slabs in Enhancing the DGS-based WPT System Performance," *2023 17th European Conference on Antennas and Propagation (EuCAP)*, Florence, Italy, 2023, pp. 1-4.

Z. Kudaibergenova, K. Dautov, and M. Hashmi, "Performance Enhancement of DGS-Based WPT System Using Double Negative Metamaterial," *2023 IEEE International Symposium on Antennas and Propagation and USNC-URSI Radio Science Meeting (USNC-URSI)*, Portland, OR, USA, 2023, pp. 547-548.

Z. Kudaibergenova, K. Dautov, and M. Hashmi, "Compact metamaterial-integrated wireless information and power transfer system for low-power IoT sensors," *Alexandria Engineering Journal*, vol. 92, pp. 176–184, Apr. 2024.

Chapter 1 - Introduction

The growing demand for electrical energy propels the modern world toward advancements in more efficient and secure approaches for gathering, converting, and transmitting power. In this context, wireless power transfer (WPT), denoting the conveyance of energy without the employment of physical wires, has gathered considerable attention across a variety of research and industry applications [1-3]. The concept of electrical energy transmission through the air medium arose in the late 19th century [4, 5]. It is important to note that the Nikola Tesla was the first person who successfully demonstrated the concept of wireless transmission in a practical experiment by lighting the tube through the capacitive coupling [4-7]. Later, Tesla presented the WPT with the help of electromagnetic induction over a relatively large transfer

distance. However, the results of the experiments demonstrated the low efficiency of power delivery. The absence of financial support and high-quality equipment shifted the research of WPT over a long period [5, 7]. Nevertheless, the performed persuasive justification of the concept possibilities led to the high interest and evolution of the WPT field to the present day.

Nowadays, electric-dependent technologies are rapidly expanding, driving the innovation of new methods to power electrical devices. Particularly, the tremendous potential of WPT systems to provide effective and practical charging has upsurged interest across multiple sectors. As a result, there is a notable rise in the quantity and diversity of established WPT systems day by day [8-10]. These technologies are represented by a transmitter (Tx) responsible for energy transfer to a receiver (Rx), separated at a specific distance [2, 3]. The WPTs enabling wireless powering can be extensively employed in fields such as medical body area networks (MBAN) [11], electric vehicles [12], consumer electronics [13], Radio Frequency Identification (RFID) [14], unmanned aerial vehicles (UAVs) [15], and Internet of Thing (IoT) devices [16].

It is worth noting that the near-field (nonradiative) WPT systems have great promise in the various domains mentioned above due to their effective power delivery over relatively short transmission ranges [8, 17, 18]. This WPT-type utilization has the potential to offer a more adaptable and simplified approach by getting rid of wires, causing energy losses and safety risks [7, 8 17]. Thus, significant research has been conducted to realize WPT systems with unique properties tailored to a variety of applications. It is important to highlight that the development of near-field systems can be achieved through the employment of coil, planar, and defected ground structure (DGS) approaches, where each demonstrates certain advantages [8, 9, 15]. Relatively long transmission distances accompany the former two methods, but they also have constraints in the form of a large system size [5, 19]. Hence, the bulky dimensions set limitations to the applicability of WPT based on coil and planar methods. Whereas the DGS approach is widely recognized for its simplicity in the design and miniature system, following a short transfer range

[15, 18]. However, It is essential to note that the issues with power transfer efficiency (PTE) arise in each design implementation of the WPT system based on any methods.

The DGS-based WPT system established in [20] featured 20 20 mm^2 × Tx and 10×10 mm^2 Rx resonators. Specifically tailored to charge implants and embedded sensors, this system was designed to operate at an optimal frequency of 50 MHz. The developed WPT demonstrated a PTE of 74% in the simulations and 68% in the measurements at the 10 mm transfer range. Another reported WPT in [21] was developed using a Tx of 31.5 31.5 mm^2 × and Rx of 10.3× 10.6 mm^2, separated by the 10 mm. The measured PTE reached 53%, while the simulated one was 58% at 40 MHz. Based on the findings, it becomes clear that simulated PTE exceeds the experimental results. This trend, where WPTs exhibit promising results in simulations but demonstrate lower performance during experiments, is observed in numerous recently published

studies [22-24]. It is important to emphasize that multiple inevitable factors lie behind the process of fabrication and measurement that can significantly influence the overall system operation. In addition, the increase in the transmission distance and occurring misalignments in the measurements contribute to the poor results [15]. On the other hand, the system size enlargement positively influences the PTE but also leads to constraints on its applicability due to the resulting bulky structure. Subsequently, various strategies are developed focusing on performance enhancement of WPT systems. In this regard, the employment of metamaterials emerges as a viable solution to cope with the aforementioned challenges.

Metamaterials (MTMs) are artificially engineered materials that demonstrate electromagnetic characteristics not found in nature, i.e. negative permeability (μ) and/or permittivity (ε) [10, 25]. It is crucial to emphasize that they are comprised of small period structures known as unit cells [10]. The design of unit cells and their arrangements play a significant role in the capability to manipulate electromagnetic waves effectively. For example, the authors in [17] proposed the MTM slab composed of 2×2 spiral unit cells, working at 6.78

MHz and 433 MHz resonant frequencies. The addition of the MTM slab of 300-by-300 mm^2 size into the multi-scale WPT system led to the rise of efficiency from 5.42% to 50.12% at 50 cm and 6.78 MHz, while at the same time from 0.72% to 3% at 2.5 m and 433 MHz. Meanwhile, the MTM in [26], having the 80-by-80 mm^2 area, was inserted in front of each Tx and Rx resonator. The WPT system, operating at the 30 mm distance and 472.6 MHz, presented a PTE rise of 8.6% with MTM inclusion. Thus, the integration of MTM has the potential to enhance the WPT performance. Apart from the PTE, the MTM shows promise in extending the transmission distance, as reported in [13]. The proposed staked MTM in [13] was integrated into the WPT system to extend the transfer range. Specifically, the developed WPT, featuring 30 30 mm^2 × size,

presented an 89.5% PTE at the 20 mm distance. The incorporation of staked MTM resulted in operation at 80 mm, which is associated with a 300% growth in the transfer range. Hence, MTMs can be effectively utilized in strategies to increase transfer range and PTE. However, it is worth noting that the majority of the reported MTMs exhibit a large area, posing inconvenience and potential challenges for small-scale applications.

This thesis work focuses on developing miniature and efficient WPT systems with a particular concentration on the performance enhancement strategy with MTM slabs and advancing the state-of-the-art in the WPT field. It is essential to mention that the *CST Studio* and *ADS softwares* were aptly utilized in all processes of design and implementation. In addition, this thesis work is divided into four chapters and organized in the following way. Chapter 2 comprehensively elaborates on the WPT system categories, power transfer techniques, and design development methods. The first section of Chapter 3 examines the realization of the WPT system with integrated biological tissue tailored to the biomedical field. Afterward, the focus shifts to the design of flexible and compact DGS-based WPT and the evaluation of the bending effect on the system performance. The third section presents the WPT with incorporated MTM of various array configurations. The WPT system in the fourth section considers the compact MTM design and

addition for PTE enhancement. The final work presented in the fifth section of Chapter 3 elaborates on wireless information and power transfer (WIPT) system design, having dual-band functionality. The availability of two frequencies makes possible the simultaneous transfer of data and power. Then, the dual-band double negative (DNG) MTM is developed for the performance improvement stage. The area of the Tx, Rx, and designed MTM are kept identical to maintain the overall miniature of the system. In conclusion, Chapter 4 briefly summarizes this thesis and discusses future perspectives.

Chapter 2 - Literature Review

2.1 WPT Categories

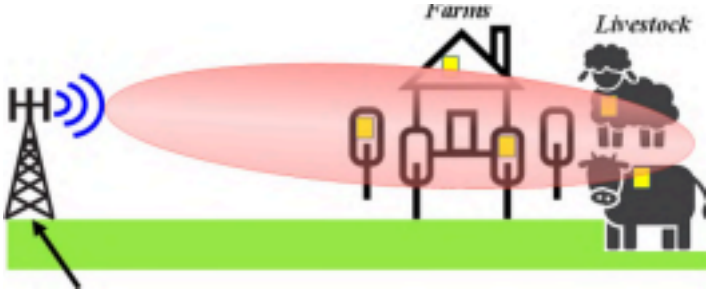

Figure 2.1: Far-field WPT system for IoT applications. Adapted from [28, Figure 1] In general, there are two distinct categories of the WPT systems, known as far-field and near-field. Far-field WPT systems operate on the principle of radiative energy transmission, allowing for efficient delivery of electrical energy over considerable distances, reaching several kilometers [4, 7]. It is essential to highlight that the wavelength of electromagnetic (EM) waves is notably smaller than the transfer range in far-field systems [27]. Consequently, these waves can propagate freely over long ranges without significant decay, making such WPTs particularly valuable in satellite communication and military applications [7, 27]. Nevertheless, efficient far-field systems are constrained by high development costs, safety concerns, and bulky sizes [7]. In this regard, recent investigations have been focused on the low-power far-field WPTs realization for employment in harvesting, sensing, and communication applications [7, 28-30]. For instance, the authors in [28] examined far-field WPT enabled by an ultra-compact and highly efficient Huygens rectenna,

specifically suitable for IoT applications, as shown in Fig. 2.1. Functioning as both an antenna and rectenna, this design presented a peak gain of 4.58 dBi at 915 MHz, while AC to DC conversion efficiency achieved 87.8%. On the other hand, the far-field WPT in [29] is developed using the transmitting horn antenna, operating at 2.45 GHz. Additionally, the gradient refractive index lens MTM is integrated into the WPT to improve the PTE at 6 m. This developed system targets applications such as UAVs, sensors, and robots.

Figure 2.2: Near-field WPT system for biomedical implants. Adapted from [12, Figure 19]

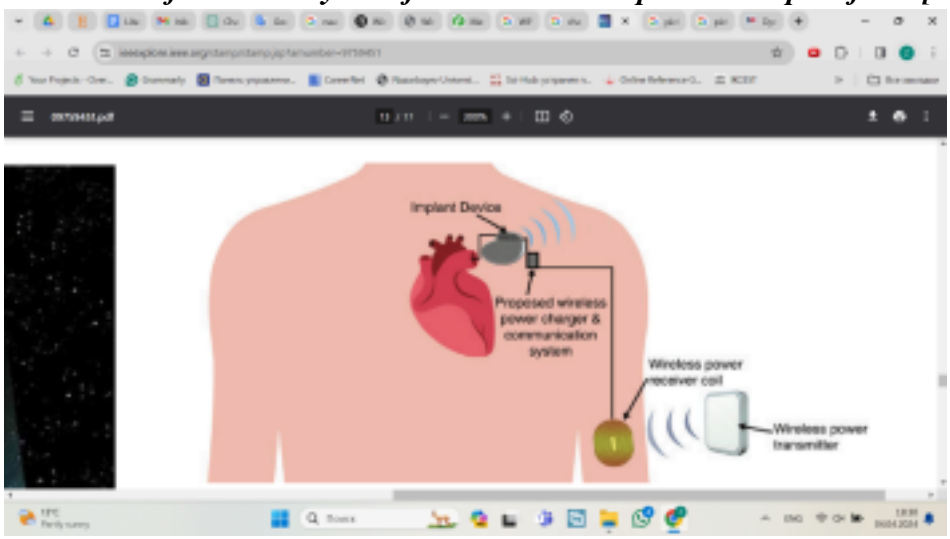

Near-field WPT systems have gathered notable attention in research and industry sectors, primarily owing to their unique capabilities and non-radiative nature. It is pertinent to mention that the wavelength of EM waves in such WPTs is significantly larger than the transmission range [27]. Therefore, near-field systems excel in delivering power over relatively short transmission distances as demonstrated in Fig 2.2. These factors collectively contributed to the growing potential of near-field WPTs in RFID, consumer electronics, UAVs, biomedical implants, IoT devices, and low-power sensors. A good example can be observed in a [31] study, where the implementation process of a near-field WPT system, working at 438.5 MHz, is presented. In detail, the two concentric open-loop spiral resonators were coupled at the 31 mm distance and showed a 70.8% PTE. Another successfully realized near-field system was presented in [6] for Ultra-High Frequency RFID application. The two identical H-shaped DGS-based resonators were separated by 8 mm and demonstrated 70% PTE at 880 MHz. Meanwhile, the authors in [32]

developed near-field inductive WPT, functioning at two ISM bands. The system consisted of modified loop antennas at both the Tx and Rx sides. Moreover, a homogenous phantom, representing the human body, is integrated into the system to enhance its suitability for biomedical applications. Considering the aforementioned advantages of the nonradiative WPT and challenges related to the radiative type, the thesis work focuses on implementing the near-field systems.

2.2 Power Transfer Techniques

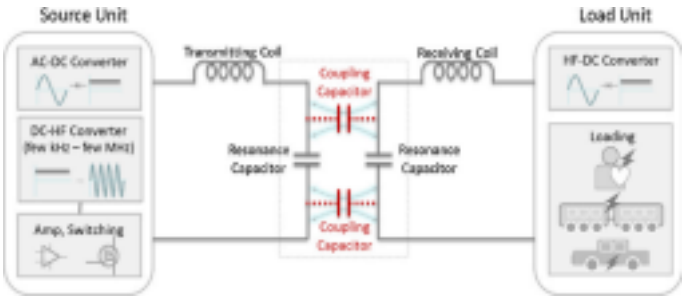

Figure 2.3: Capacitive power transfer. Adapted from [5, Figure 2]

The realization of the WPT can be accomplished by the electric coupling related to the capacitive power transfer (CPT) or magnetic coupling associated with inductive power transfer (IPT) and magnetic resonant coupling (MRC) [4, 27]. The development techniques are selected depending on the application's requirements. It is important to mention that the CPT method considers capacitive coupling between two metallic plates to transfer power wirelessly [27]. In other words, AC voltage applied to the Tx produces the electric field between electrodes, which further induces the voltage on the Rx side, as depicted in Fig. 2.3 [5, 33]. The advantages of this method include minimal power losses, robustness to misalignment, and less generated heat, while the drawbacks contain limitations on mobility and design flexibility [27, 33]. The CPT technique is mostly utilized for short-range applications, while the increase in the transfer distance requires high voltages and frequency. Despite the proposed advantages, this method has not been extensively researched [5, 27].

In the IPT case, the electric energy is transferred through the magnetic field between two

coils. To make it more clear, when AC flows through the Tx side, it produces a varying magnetic field (H-field), which in turn, induces the voltage on the Rx side, as can be seen in Fig. 2.4 [5, 27]. It is pertinent to note that this approach's advantages are robustness, design flexibility, and

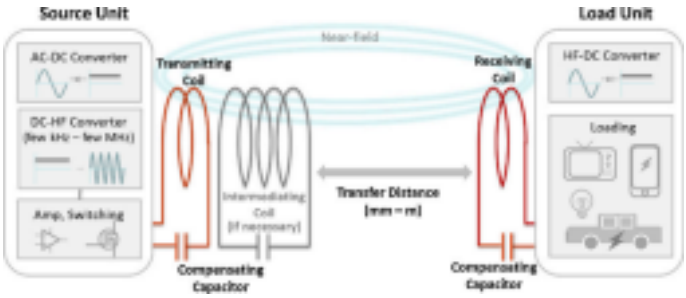

Figure 2.4: Inductive power transfer. Adapted from [5, Figure 1]

safety, while the disadvantages include realization costs, power losses, and misalignment issues [4, 27]. The IPT technique is mostly utilized for short to medium distances, and when the transfer range increases, the PTE inversely reduces. It is worth mentioning that the IPT concept can be further expanded to the MRC method, which is also based on the same principle [5, 27]. In the case of MRC, both Tx and Rx resonators are designed to function at identical resonant frequencies, positively influencing the system performance. This approach offers increased transmission distance and more stable performance with the impact of environmental factors in the form of displacements. In both approaches, it is crucial to determine the perfect coupling condition for reaching the highest energy transmission. Concerning the proposed advantages, the MRC is subsequently applied in the WPT systems' realization process.

2.3 Design Development Methods

The quantity of the realized WPT system is rapidly growing as its design diversity. In general, the development of the WPT system can be accomplished using different design approaches: the coil, planar, and DGS. Here, the former technique mostly utilizes the inductive coupling between Tx and Rx coils [4, 34]. Furthermore, the coil-based WPT system has various

design configurations, i.e. 3D structures, solenoids, etc. The parameters of the coil, in the form of the material, the number of turns, the width of the spirals, and the radius of the coil considerably

Figure 2.5: Coil-based WPT system measurement. Adapted from [34, Figure 15] impact the resonance occurrence, PTE, and transfer distance [34, 35]. The simple design process and configuration considerably contributed to the widespread utilization of the technique and the growth of various developed coil-based WPTs. Authors in [34] developed the system based on the mentioned approach, as depicted in Fig. 2.5. The coil-based system was accurately designed using the particle swarm optimization algorithm and modified AC resistance evaluation method. All this notably impacted the coil-based WPT system, which demonstrated an electric energy transfer efficiency of 95.6%, while the conventional design is 94%. Another reported WPT system in [35] employed superconducting coils. It is detected that the superconducting coil is associated with a higher quality factor and PTE in comparison with traditional coils. The WPT system based on superconducting coils resulted in the growth of PTE up to 40%. The planar approach is well-known for its reliable performance in short-range distances. This technique is broadly developed using the printed circuit board (PCB) or other planar substrates [16, 26, 36]. The dimensions of the planar coil represented upfront to the substrate have a significant influence on the overall system performance. Thus, there is various research conducted on the realization of the efficient planar-based WPT system [19, 26, 36]. One of the planar-based WPTs' realizations is presented in [16]. The system is implemented using two identical hexagonal-type antennas, having 48-by-44 mm^2 areas and operating at 433 MHz. The

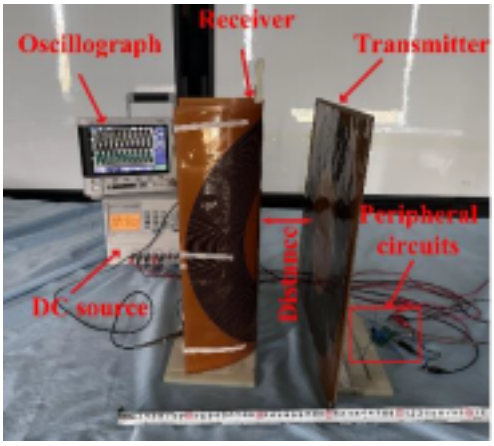

Figure 2.6: Planar-based WPT system measurement. Adapted from [36, Figure 2]

developed WPT presented a PTE of 90% at the separation range of 23 mm. Apart from the traditional planar method, considerable research has been conducted on the hybrid technique, where different planar coil configurations are used in the WPT implementation. The performed study in [36] established WPT based on the planar and cylindrical coils, introducing the gain element source and the concept of parity-time (PT) symmetric, as illustrated in Fig. 2.6. The realized system demonstrated robust transmission over a 100 mm distance and 80.3% PTE. Furthermore, the performed study revealed and verified that planar coil Tx and cylindrical coil Rx can maintain relatively stable efficiency in the strongly coupled region regardless of the PT symmetry, contributing to a robust wireless charging technology field.

In recent times, the employment of the DGS method has been broadened, owing to the numerous benefits offered. As reported in [15, 20], this approach is renowned for its simple design process and the resulting miniature structure. For instance, authors in [14] proposed a dual-band DGS-based WPT system operating at industrial, scientific, and medical (ISM) bands. In this work, the defect shape of the resonator is represented by the overlapping circular slots, which are employed for reaching the high compactness and Figure of Merit (FoM). The 11.7× 10.2 mm^2resonators are placed apart by 15 mm and showed a 40.9% and 49.2% PTE at 440 MHz and 918 MHz, respectively. Meanwhile, the system in [37] is developed using resonators,

Figure 2.7: DGS-based WPT system measurement. Adapted from [37, Figure 19]

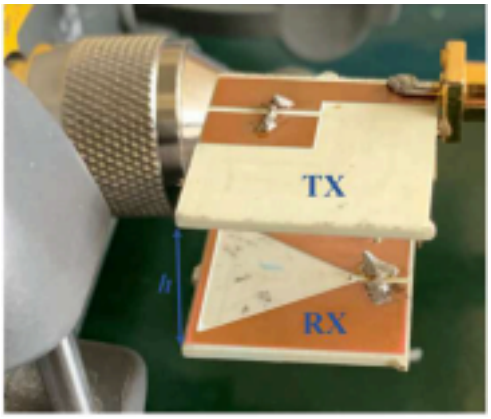

containing the triangular shape defect and size of 20-by-20 mm^2. At the distance of 17 mm, as depicted in Fig. 2.7, the PTE achieved a value of 80% at the 300 MHz frequency. According to the published works, the DGS technique can be apt

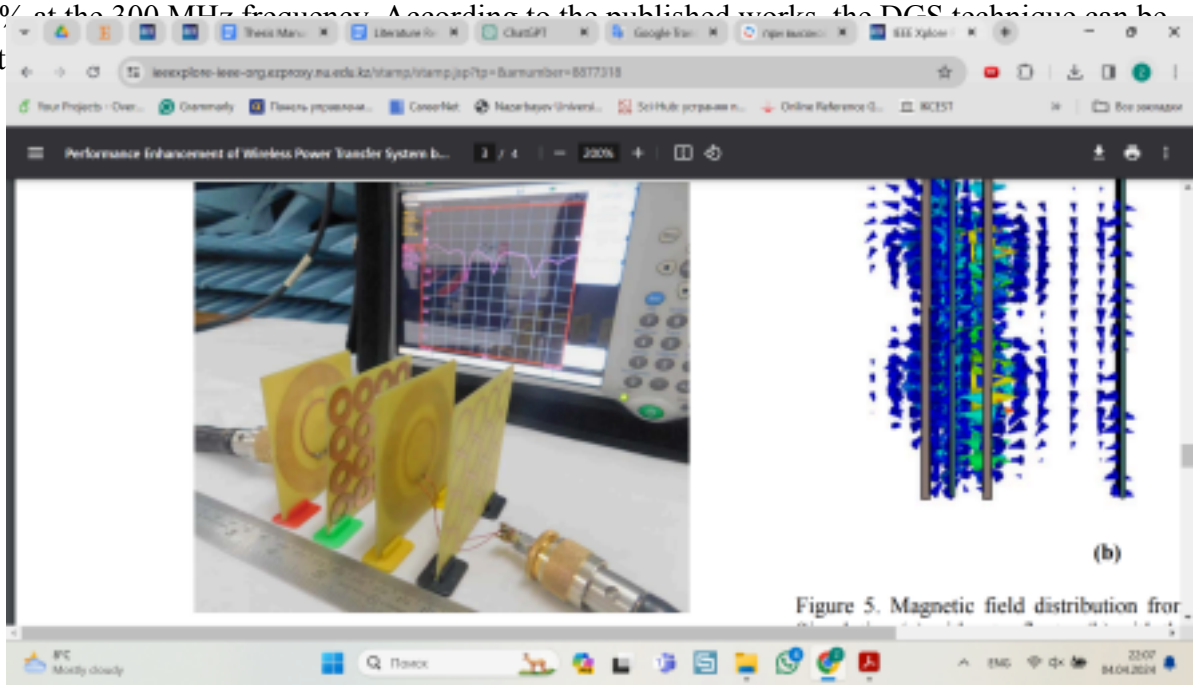

2.4 Metamaterial

Figure 2.8: Measurement of WPT with integrated MTMs. Adapted from [19, Figure 4]

Nowadays, the MTMs' importance is great due to their unique unnatural properties [10, 13, 17, 25]. As was previously mentioned, the MTM is an artificial periodic slab, composed of unit cells, and possesses negative permeability and/or permittivity [26]. The unit cell design noticeably

influences the appearance of negative properties and the majority of the recent

structures have been realized using the split-ring resonator (SRR) structures. It is pertinent to highlight that the MTM can be developed to manipulate magnetic field lines, enabling precise control over the direction and focus of the energy transfer [13, 17, 19]. By designing the MTM slab appropriately, it is possible to concentrate the magnetic field, directing it more efficiently toward the Rx resonator. This concept has been investigated in numerous works, which considerably influenced the diversity of different MTM designs and demonstrated their usefulness in performance improvement approaches.

The recently realized MTMs have demonstrated strong potential in enhancing the PTE of WPTs. For instance, authors in [19] conducted the performance enhancement of WPT by controlling transmission and MTM reflection characteristics. Fig. 2.8 demonstrates the realized WPT and integrated 4×4 MTM slabs. The incorporation of the engineered material led to the 15% PTE improvement at the 10 mm transfer range. On the other hand, the study performed in [38] involved the realization of the ultra-thin and extremely subwavelength magnetic MTM appropriate to the 13.56 MHz WPT system for enhancing H-field and PTE. The designed MTM addition resulted in an increase of the PTE by 36.4%. Another notable example of the artificial material utilization was recorded in [39]. Here, the MTM with 2×2 array configuration was added between the Tx and Rx sides at different positions. According to the conducted analysis, the maximum PTE improvement of up to 50% was detected, when the MTM slab was positioned in the middle of the WPT system. It is possible to conclude that the majority of the investigations confirm the usefulness and positive effects of MTM slabs in performance improvement strategies of the WPT system.

Chapters 3 - Development Methods and Obtained Results

3.1 Design of Compact DGS-Based WPT System with Integrated Biological Tissue

In today's modern world, there is a strong demand for increasingly advanced and flexible power systems tailored for healthcare applications. The prevalence of patients in need of diverse biomedical implants and wireless sensors is steadily rising. The role of medical devices in monitoring human vital health parameters, including temperature, pressure, and pulse, is significant and requires advancements in powering technologies to meet these evolving needs [3, 40]. The traditional methods of charging, in the form of wires and batteries, are associated with certain inconveniences and safety risks, including electric shock, fires, and issues related to the surgery for replacement [40, 41]. As a result, the WPT technologies demonstrate great promise in diverse device powering for the healthcare sector. Therefore, this work is centered on developing a compact DGS-based WPT system suitable for biomedical implants.

Firstly, the design process of the compact resonator, having a resonant frequency of 405 MHz, was performed to meet the specified application. Secondly, the WPT system was established by employing two identical resonators, one acting like a Tx and the other as an Rx. Furthermore, the developed system verification was completed with the integration of the biological tissue to ensure a more realistic scenario. It is essential to highlight that the introduction of biological tissue can significantly affect the WPT performance. Thus, the thickness of the tissue is increased with a 1 mm step, reaching 10 mm. Afterward, the developed WPT in the simulation domain was further fabricated to obtain the experimental results and design validity. Finally, an additional analysis of the specific absorption rate (SAR) was

conducted to confirm the appropriateness and ensure compliance with safety requirements.

3.1.1 Resonator Modeling

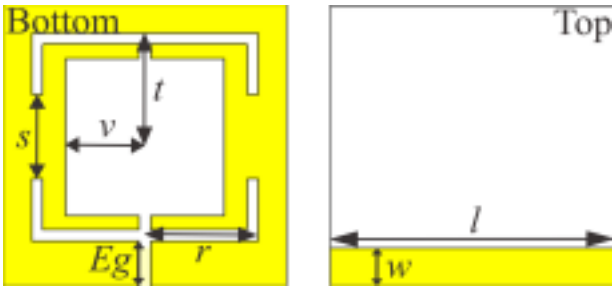

Figure 3.1: Proposed resonator

In this subsection, the realization of the DGS-based resonator is described in detail. Initially, the area of the resonator was selected to be 25 25 mm^2 × to meet the compactness requirements for biomedical implants. Fig. 3.1 depicts the geometry of the proposed resonating structure, comprising three layers. Particularly, it is composed of the 1.54 mm RO4850B substrate covered from two sides by the copper layers, each having a 0.035 mm thickness. Here, the top layer is defined as the microstrip line (ML), indicated by the length (l) and width (w). The parameters of the ML (i.e. feeding line) were selected to have the 50 Ohm characteristic impedance, resulting in l = 25 mm and w = 3.4 mm. Meanwhile, the bottom layer comprises the etched defect (i.e. etched slot) and excitation gap marked as *Eg*. It is pertinent to mention that the defect parameters can considerably impact the occurrence of the resonance. Therefore, it is possible to tune the resonant frequency (f_r) by carefully selecting the design parameters. Another method for shifting the resonance is accomplished by adding a lumped capacitor into the *Eg*.

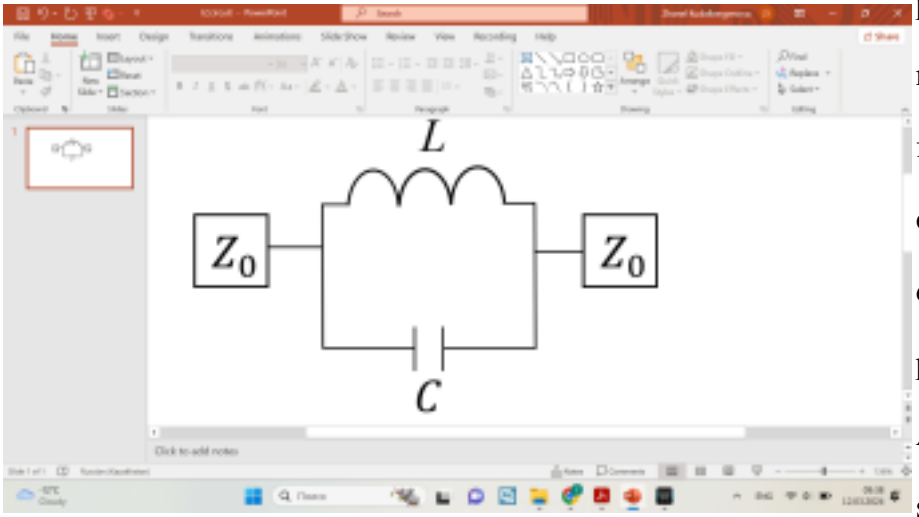

Figure 3.2: Equivalent circuit of the DGS-based resonator

Since the equivalent circuit (EC) of the DGS-based resonator is represented by *parallel LC*, shown in Fig. 3.2, the variation of the defect shape responsible for inductance (L) or the capacitance (C) can result in a change of resonance. The circuit parameters of the resonator are determined by utilizing the Eqs. (1)−(2), where $Z_0$is set to 50 Ohm impedance, and f_c stands for the cut-off frequency (-3 dB) [18, 37]:

$$L = \frac{Z_0}{4\pi f_c (f_c^2 - f_{-3dB}^2)} \quad (1)$$

$$C = \frac{1}{4\pi^2 f_{-3dB}^2 L} \quad (2)$$

It is worth noting that the DGS-based resonator's defect parameters were chosen as follows: v = 7 mm, s = 7.5 mm, r = 10 mm, t = 9.25 mm, and Eg = 4 mm. Using the EM results and stated formulas, it was possible to determine the values of L and C, which are 36.5 nH and 0.74 pF. To reach the resonance at 405 MHz, it was decided to add an external capacitor (C_p), whose value was calculated by using Eq. (2) with L = 36.5 nH and further substarting the C = 0.74 pF from the obtained value. The performed computation and slight optimization led to C_p = 3.5 pF. Finally, Fig. 3.3 demonstrates the obtained EM and EC results of the designed resonator, ensuring its validity in further implementation of the WPT.

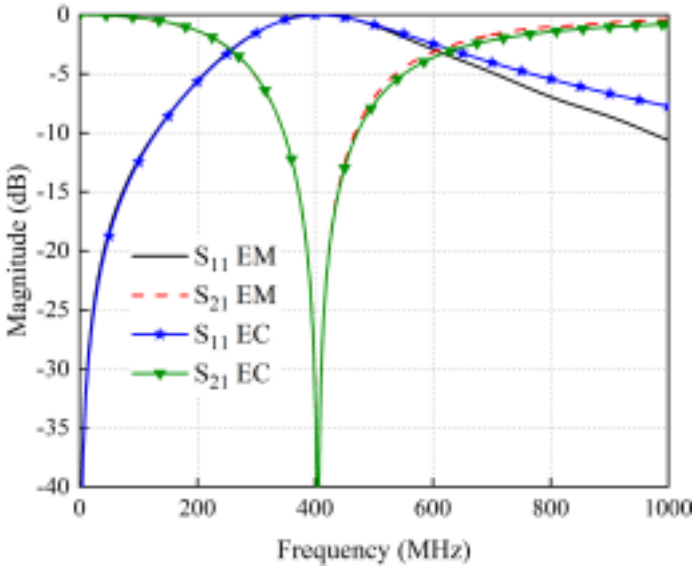

Figure 3.3: Obtained results of the DGS-based resonator

3.1.2 WPT System Realization

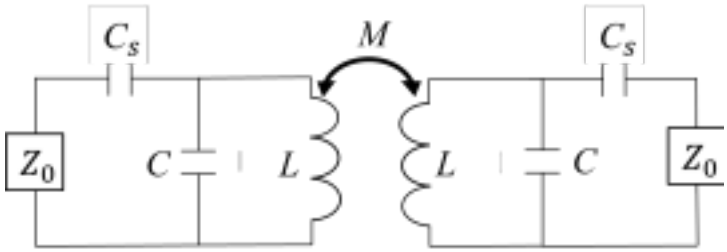

Figure 3.4: Equivalent circuit of the WPT system

Generally, the realization of the DGS-based WPT system is reached by coupling two identical resonators at the specific transmission distance. It is important to emphasize that the MRC technique was employed to reach the maximum power transfer by establishing a robust magnetic coupling between two resonators operating at identical frequencies. Moreover, the selection of the transfer distance is also a pivotal consideration. In detail, the short transfer range can lead to a frequency split phenomenon, while the large one can result in a complete decoupling of resonators. Hence, it is highly essential to precisely determine the delivery distance, which, for this particular design, was set to 20 mm. The other important factor that has to be considered is impedance matching, which is necessary for minimizing the reflections at the input port and maximizing the PTE [15]. Furthermore, the two identical resonators must work at

a similar frequency for coupling purposes. The stated impedance matching and identical resonant frequency were reached by optimization of C_p and ML length (l) values [15, 18].

Fig. 3.4 demonstrates the EC of the WPT system, where the circuit parameters are L, C,) characterizing the ML capacitance. The oyment of the equations below [14, 18]:

$$\beta = \frac{2\pi f \sqrt{\varepsilon_{eff}}}{c_0} \quad (6)$$

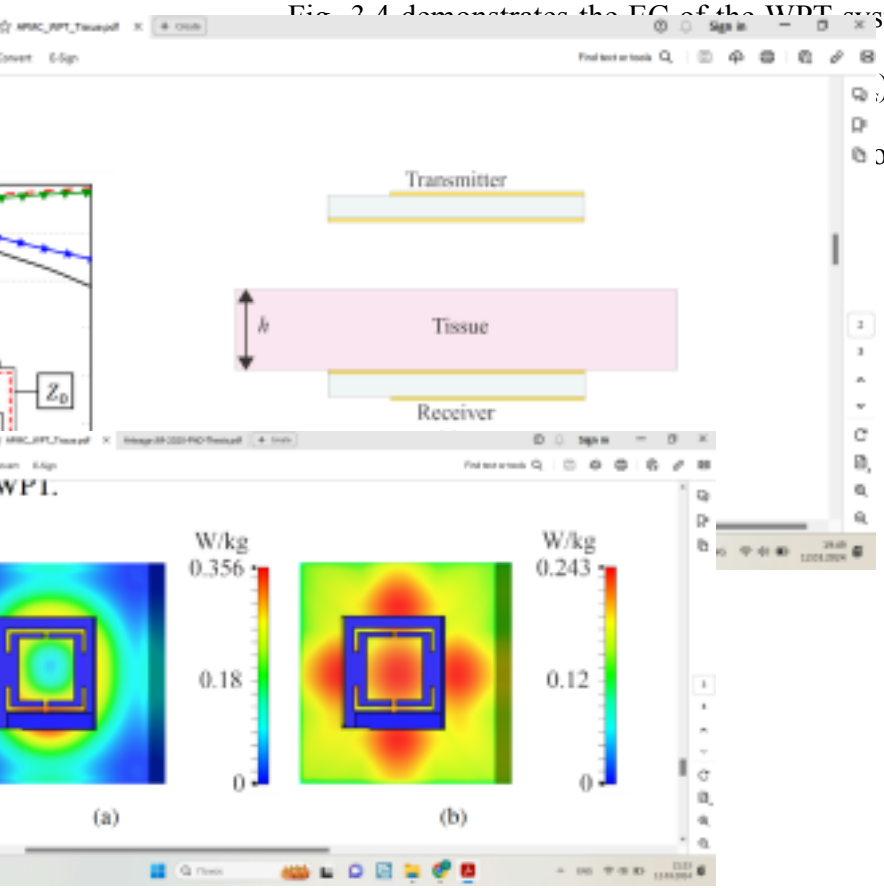

(a) (b)

Figure 3.5: Simulation process of the developed WPT system with biological tissue

(a) 1-g (b) 10-g

Figure 3.6: The SAR values of the designed system

It is worth noting that Z-parameters were defined by removing the ML from the two resonators and exciting the structures from *Eg* [18]. Further, *Im* (Z_{11}) represents the imaginary part of the impedance element $Z_{11,}$ and *Im* (Z_{21}) similarly refers to the impedance element Z_{21}. Afterward, the value of C_s is calculated with Eq. (6), where β represents the phase shift commuted using the formula $\beta = \frac{2\pi}{\lambda}$ and $\lambda = \frac{300}{f\sqrt{\varepsilon_{eff}}}$ [14, 18]. Overall, the obtained results were slightly modified and reported as follows: l = 17.5 mm and C_p = 2.4 pF.

The following stage involved the integration of the tissue, featuring a 3.16 loss tangent,

77 relative permittivity, and 0.68 S/m conductivity [20]. It is imperative to emphasize that the gradual addition of biological tissue is crucial since the presence of any material other than the air medium can considerably influence system performance [20, 40]. Any external material placed in between the coupled resonators introduces its contributions, which can be an advantage or detrimental to the WPT. Initially, the thickness of the tissue was set to 1 mm, and further, the

value was increased up to 10 mm, as shown in Fig. 3.5. The appropriate optimization in the Tx and Rx resonators accompanied each thickness rise. Subsequently, the final parameters of the resonators were determined and presented as follows: C_p = 2.65 pF and l = 20 mm for the Tx side; C_p = 2.5 pF and l = 21.5 mm for the Rx side. Furthermore, the SAR analysis was carried out, utilizing 10 mW input power, to ensure compliance with safety requirements [41]. The standard SAR value for 1-g and 10-g should not surpass 1.6 W/kg and 2 W/kg, accordingly [9, 41, 42]. Based on the results depicted in Fig. 3.6, the SAR values reached 0.356 W/kg for 1-g and 0.243 W/kg for 10-g, confirming the safety and potential for usage in the biomedical field.

3.1.3 Measurement Setup and Representation of Obtained Results

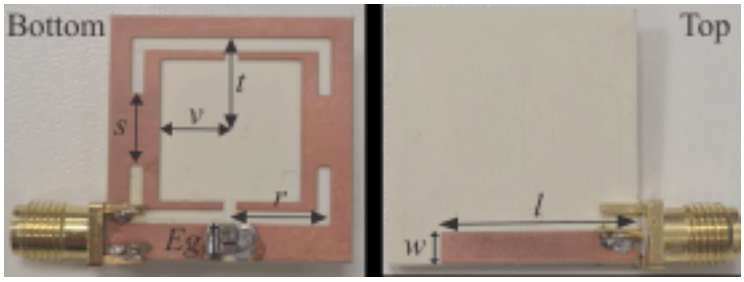

(a) (b) (c)

Figure 3.7: Fabricated prototypes of the designed resonator (a)-(b) and measurement setup (c)

This subsection comprehensively discusses the measurement setup and the experimental results.

It is necessary to highlight that in the experimental measurements, equipment such as a PCB printing machine and Vector Network Analyzer (VNA) were used for the fabrication of the resonating structure and measuring the S-parameters of the WPT system. In this process, the developed DGS-based resonators were fabricated and external SMD capacitors were soldered into the *Eg* for each Tx and Rx sides, correspondingly (Fig. 3.7a and 3.7b). Afterward, the two

Figure 3.8: Experimental and EM results of the realized WPT system

resonators were distanced by 20 mm and linked to the VNA by SMA connectors (Fig.3.7c). Apart from that, the calibration of the VNA in the range of 0−1000 MHz was conducted to ensure accurate results before the measurements. In addition, the biological tissue used in the simulation was represented by a chicken breast in the experimental setup. Lastly, It is pertinent to note that the PTE and FoM can be estimated by applying the following formulas [14, 15]:

$$\text{PTE} = \frac{1-|S_{11}|^2}{1-|S_{22}|^2} \times 100\% \quad (7)$$

$$\text{FoM} = \frac{\text{PTE}}{1-|S_{11}|^2} \quad (8)$$

Fig. 3.8 demonstrates the experimental and simulation results of the developed DGS-based WPT system with integrated 10 mm biological tissue. In compliance with the obtained results, the value of S_{11} exceeded −10 dB for both cases, indicating the perfect impedance matching. Meanwhile, the S_{21} value in EM equaled −2.87 dB leading to the 52% PTE and the measured S_{21} reached −3.4 dB, corresponding to a PTE of 46% and FoM of 0.368. The variation between EM and experimental PTE and frequency shift can be attributed to the in-house production, the influence of the external capacitors, as well as a difference in the properties of the utilized biological tissues. Overall, the demonstrated results of the designed DSG-based WPT underscore its practicality and applicability in the biomedical sphere.

3.2 Flexible DGS-Based WPT System Design for the Biomedical Field

The biomedical implant demand for monitoring human physical conditions is constantly growing. In the context of implants like pacemakers, there's promise in integrating wireless charging technology. In detail, it is envisioned that the Rx resonator will be directly embedded within the implant itself, while the Tx side is positioned close to the human body. In this scenario, the bending of the Tx has a high probability, which further has the potential to impact its overall performance. Since the WPT system is intended for healthcare, it is highly important to consider the bending effect of the resonator on the whole WPT operation. Thus, this section focuses on the development of a miniature and flexible DGS-based WPT system tailored to biomedical applications. To reach the stated objectives, the resonator design envisaged the employment of a flexible substrate. The WPT system realization was conducted in two approaches with unchanged resonators and with a bent Tx side. Subsequently, the impact of bending on the system work was evaluated and compared.

3.2.1 Development of the Resonator Based on a Flexible Substrate

Fig. 3.9 shows the DGS-based resonator geometry, having the 22 22 mm^2 × compact size. The composition of the proposed resonator is as follows: 0.79 mm RT5880B flexible substrate and two copper layers with a thickness of 0.0175 mm. In the presented design, the top side consists of the ML with parameters w = 3.4 mm and l = 22 mm. On the other hand, the bottom side contains the etched slot, represented by the hexagon spiral shape with the following parameters: a = 1 mm, b = 0.5 mm, and n = 4 standing for the number of turns. In addition, there is also an excitation gap with a width of 0.5 mm and a length of 3.25 mm. Since the overall the

(a) Bottom (b) Top

Figure 3.9: Geometry of the flexible DSG-based resonator

system is expected to be applied in the biomedical sphere, the operation of the flexible resonator based on DGS should be in the ISM band, specifically at 405 MHz. Consequently, the external capacitor is integrated into the system to reach the desired working frequency. It is worth mentioning that the EC of the resonator based on the flexible structure is similar *to parallel LC* (Fig. 3.2). Therefore, the computation of the $C_p$is identical to the process demonstrated in 3.1.1. subsection, which resulted in a C_p of 4.15 pF. Lastly, Fig. 3.10 illustrates the EC and EM results of the designed resonator based on DGS, which are in perfect agreement at 405 MHz.

Figure 3.10: EC and EM results of the resonator

3.2.2 Design of the Miniature and the Flexible WPT System

(a) Case 1 (b) Case 2

Figure 3.11: Two scenarios of the DGS-based WPT performance verification As mentioned earlier, the WPT is constructed using two resonators separated by 20 mm, where one serves as Rx and the other Tx. The designed structure in the former subsection was used in the system's development process. It is imperative to highlight that the modifications of the ML parameter and C_p were required to attain impedance matching and functioning at the frequency of interest. The computation of the key parameters followed the same approach as described in subsection 3.1.2. Based on the calculation results, the C_p and l were determined to be 2.65 pF and 24.5 mm, respectively. Since the maximum length of the ML attained 22 mm, the remaining 2.5 mm was added vertically to one end of the feeding line. Afterward, the optimized DGS-based resonators were separated by the 20 mm transmission distance. It should be noted that the verification process of the designed flexible WPT system entailed two distinct cases. In detail, Case 1 involved the measurement of the developed system without any modifications, whereas Case 2 considered the performance verification with a bent Tx resonator from two sides and an unchanged Rx side. Fig. 3.11 demonstrates two scenarios with h, representing the power delivery distance, set to 20 mm. Eventually, the simulation was carried out and results were provided in the subsequent subsection.

3.2.3

Experimental Measurement and Results Discussion

(a) Bottom (b) Top (c) Case 1 (d) Case 2 Figure 3.12: Two scenarios of the DGS-based WPT performance verification

(a) EM (b) Experimental

Figure 3.13: Obtained results of the miniature and flexible DGS-based WPT system Fig. 3.12a and 3.12b present the manufactured prototypes of the designed resonator with soldered SMD capacitors and SMA connectors. The measurements were carried out for two cases in both simulation and practical experiments, showcased in Fig. 3.12c and 3.12d. It is important to emphasize that the EM and experimental results are approximately identical, as depicted in Fig. 3.13. From the received results, it is evident that S_{11} exceeds −10 dB, specifying the attained

impedance matching for each case. In the measurement results, S_{21} for Case 1 equals −1.73 dB, related to the 67% PTE, and Case 2 is associated with S_{21} of −2.1 dB, corresponding to a PTE of 61%. Based on the findings, it can be concluded that the bending effect negatively

affected the PTE. Particularly, the PTE of the flexible WPT system based on DGS decreased by 6% with the bending of the Tx resonator. Concerning the resonance occurrence, a small shift in the resonant frequency was possible to observe, which is at an acceptable level. Overall, the realized compact and flexible DGS-based WPT performance validates the potential and current perspective in biomedical field employment, also indicating the negative impact of bending.

3.3 Development of the DGS-Based WPT System and Performance Enhancement through Metamaterial Integration

At present, the quantity of WPT systems is increasing at a high rate with the demand for innovation in various applications. Nevertheless, issues with PTE exist in the majority of the reported designs since the experimental measurements demonstrate low performance. It should be highlighted that there are different inevitable factors, including losses due to the environmental conditions and equipment used, impacting the overall WPT performance. Therefore, it is crucial to devise efficient strategies aimed at enhancing the systems' PTE. In this regard, MTMs also known as artificial materials showcase the potential to improve the power delivery capability by redirecting the H-field lines. Hence, this work aimed to develop a miniature WPT system and employ the performance enhancement strategy centered around MTM. Initially, the focus was directed towards realizing the fundamental element of WPT, i.e. resonator, functioning at 900 MHz, and further to the WPT based on DGS design. Subsequently, the development of an MTM basic block, known as a unit cell, was conducted, which was then utilized in the creation of MTMs with 2×2 and 3×3 arrangements. At last, the WPT system performance was validated

with and without MTMs addition at 19 mm.

3.3.1 Resonator Realization

(a) Bottom (b) Top

Figure 3.14: Geometry of the flexible DSG-based resonator

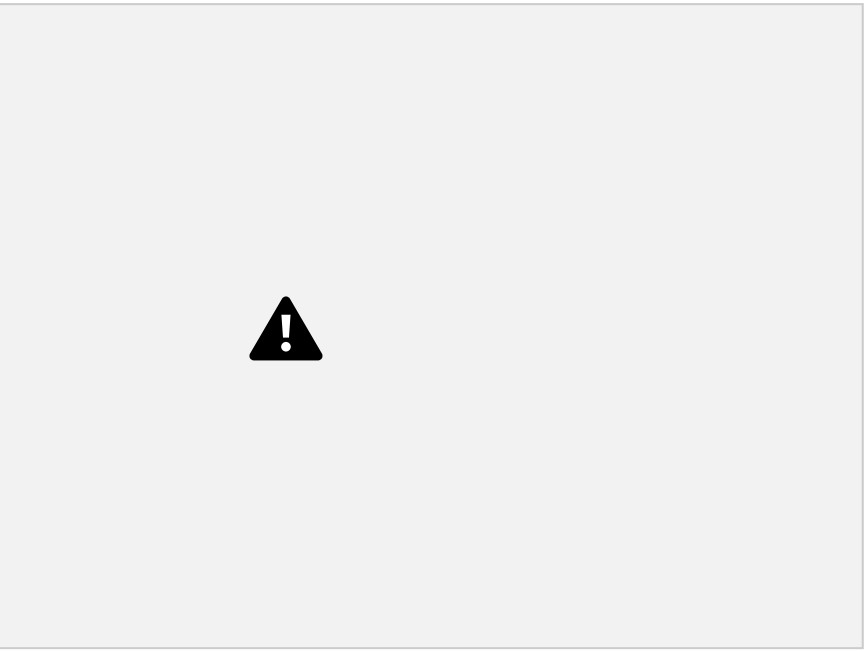

Figure 3.15: EM and EC simulation results of the designed resonator

The design of the fundamental element of WPT is extensively examined in this part. Fig. 3.14 demonstrated the DGS-based resonator with a board area measuring 20-by-20 mm^2. The

resonator composition is similar to the one provided in subsection 3.1.1. In this proposed design, It is possible to observe that the complex defect shape and *Eg* with 1 mm width are located at the bottom layer. In detail, the etched defect with the ornament pattern is indicated in the structure with parameters as follows: a = 19 mm, $b = c$ = 4 mm, d = 3 mm, and e = 2 mm. In addition, the top layer is composed of the ML, featured by w = 3.4 mm and l = 20 mm, and two excitation ports presented as P1 and P2. Furthermore, the proposed resonating structure was designed and

expected to work at 900 MHz frequency, included in ISM. To attain the desired operation, the external C_p of 0.3 pF value was added into the *Eg*, leading to the EM and EC results illustrated in Fig. 3.15. The perfect matching of the two results prompted the employment of the developed resonating structure in further WPT realization.

3.3.2 WPT System Development

Figure 3.16: The WPT system's EM results

The WPT system establishment involves two resonators coupling, followed by their separation within the optimal transfer range, which is 19 mm for this specific design system. It is essential to emphasize that the proposed design of the resonator successfully achieved resonance at 900 MHz, thereby eliminating the need for additional lumped elements. Concerning

impedance matching, the optimum length of the feeding line for maximum power delivery was estimated to be 11.3 mm. Afterward, the WPT system was implemented using the optimized DGS-based resonators, with a transmission range set at 19 mm. From the EM results in Fig. 3.16, the designed WPT perfectly operates at 900 MHz and shows good impedance matching since the $S_{11} < -10$ dB. At the same time, the S_{21} equals −2.6 dB, resulting in an approximate 57% PTE.

3.3.3 Design of the Unit Cell and Metamaterials with Different Arrays

Figure 3.17: Unit cell structure

Figure 3.18: Unit cell result: permeability vs frequency

The realization of the MTM structure begins with the design of its basic block, i.e. unit

unit cell arrangements. It

emonstrate the negative

developed system in the

the development of the

fied objectives, the SRR

he proposed unit cell

(a)2×2 (b)3×3

Figure 3.19: MTM configurations with different arrays

design, comprising two concentric metal rings placed on the substrate with the metal wire from the other side. It is worth mentioning that the unit cell has a 20 20 mm^2 × area with a material composition similar to the resonator. With respect to the design parameters, m = 0.5 mm stands for the rings' width, n = 0.23 mm constitutes the spacing between rings, R = 9.5 mm represents an outer radius, t = 0.5 mm, and v = 2 mm are widths of split and metallic wire, accordingly. In the design process, It was possible to detect that the variation of n and t can significantly impact the resonant frequency, particularly resulting in the occurrence of the resonance at lower frequencies. As a result, the values of the provided parameters were carefully selected and adjusted to ensure the negative μ at the desired range.

It is apparent from Fig. 3.18 that the negative μ is achieved around 900 MHz with the proposed unit cell design. Therefore, it is conceivable to assert that this unit cell design holds the potential for further utilization in MTM assembling. Afterward, Fig. 3.19 demonstrates the MTM structures assembled in the 2×2 and 3×3 array configurations. Eventually, the following subsection extensively reviews the integration process of the developed MTM slabs of the 2×2 and 3×3 arrangements into the DGS-based WPT system for achieving the purpose of performance improvement.

3.3.4 Integration of Metamaterials into the DGS-Based WPT System

Figure 3.20: The performance validation of the WPT system with integrated MTM

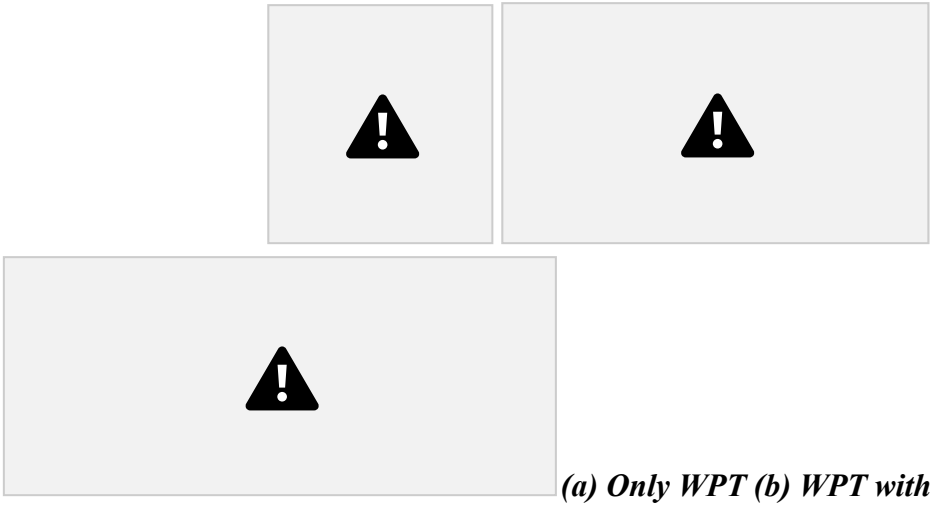

(a) Only WPT (b) WPT with 2×2 MTM (c) WPT with 3×3 MTM Figure 3.21: The generated H-field

This subsection examines the verification process of the WPT system performance with and without the MTM addition. In this work, the position of MTM slabs was chosen at the center between the Tx and Rx resonators, as depicted in Fig. 3.20. This strategic positioning of MTM ensures maximum interaction with the H-field and uniform energy distribution. It is crucial to mention that the misalignment in WPT considerably degrades the operation, leading to the shift of resonant frequency and reduction of PTE. Consequently, the placement of Tx and Rx with the MTM in the middle should be aligned to reach the maximum energy transfer.

The produced H-field of the WPT system with and without incorporated MTM slabs is demonstrated in Fig. 3.21. Apparently, the addition of MTM slabs results in the enlargement of the H-field around coupled resonators. Apart from that the MTM with a 3×3 array presents the

Figure 3.22: PTE of three scenarios

largest expansion of the H-field. Hence, one can assert that the larger the integrated MTM area, the greater the H-field enlargement. Apart from the H-field, the improvement of PTE is also detected in the obtained results. Fig. 3.22 presents the PTE of the three scenarios: (1) only WPT system, (2) WPT with 2×2 MTM, and (3) WPT with 3×3 MTM. Based on the obtained outcomes, 2 and 3 scenarios corresponded to PTE of 64% and 68%, respectively. The

performance of the DGS-based WPT was significantly enhanced with 3×3 MTM incorporation, particularly by 11%. As a result, the MTM addition into the WPT system is accompanied by H-field enlargement, contributing to the PTE improvement.

3.4 Establishment of WPT System with DNG Metamaterial Addition

In the realm of biomedical applications, the wireless powering capability has the potential to simplify the variety of medical devices' charging greatly. Nevertheless, the performance of the WPT system incorporated into the implants like pacemakers, can be significantly affected by environmental conditions. Therefore, enhancing the operation of the DGS-based WPT system is vital, and the MTM integration can serve as a promising and effective strategy to achieve this

goal. However, the majority of published works have highlighted the prevalence of MTMs with considerable size, making the overall system bulky. Thus, this study was focused on developing a WPT system based on DGS and incorporating a compact DNG MTM to enhance performance. It is pertinent to note that the miniature DNG MTM was designed by using only one unit cell of resonator size. Hence, the overall WPT system with integrated MTM is considered practical and compact for usage in the biomedical area.

3.4.1 Resonator Development

Figure 3.23: Proposed resonating structure based on DGS

The design process of the resonator began with a board area selection that is 30 30 mm^2 ×

for this work. The DGS-based resonator maintains the same material structure as previous designs, utilizing RO4350B substrate. Concerning the layers' composition illustrated in Fig. 3.23, the top side consists of the feeding line, characterized by w = 3.4 mm and l = 30 mm. Meanwhile, the bottom layer contains the defect shape formed by two circles and Eg of 3.51×1 mm^2 dimensions. The defect design parameters are as follows: p = 2 mm, q = 1 mm, K = 11.5 mm, and k = 8 mm. In addition, the proposed structure resonant frequency was set at 405 MHz. As a result, the lumped capacitor of 3.6 pF was incorporated into the circuit, particularly to Eg. It is essential to note that the calculation of the external element was accomplished in the way

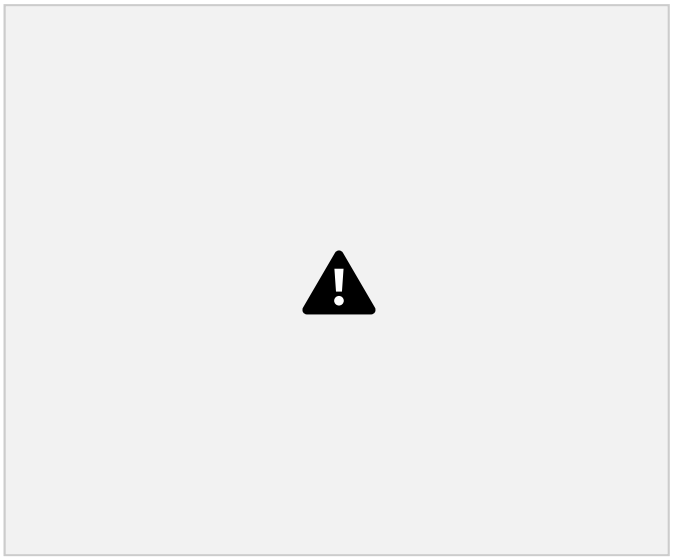

Figure 3.24: Proposed resonating structure based on DGS

demonstrated in earlier structures. In conclusion, the capacitor integration led to the EM results shown in Fig. 3.24, ensuring the resonator utilization further.

3.4.2 Coupling-Based WPT System Design

The realization of the DGS-based WPT system is extensively discussed in this subsection. Consistent with previous designs, the WPT system is configured such that the Tx and Rx are positioned 50 mm apart. Moreover, the crucial point in the design procedure is to ensure impedance matching to minimize losses during the power transfer, which is achieved by

determining the appropriate length of the feeding line. Additionally, the performance of WPT should be at the desired frequency. To meet the stated requirements, the *J*-inverter approach was appropriately employed to compute the optimization parameters. In general, this technique is widely utilized for impedance matching due to its accuracy and efficiency [11]. Fig. 3.25 presents the EC of the WPT system, using the *J*-inverter technique [11, 12]. In the computation

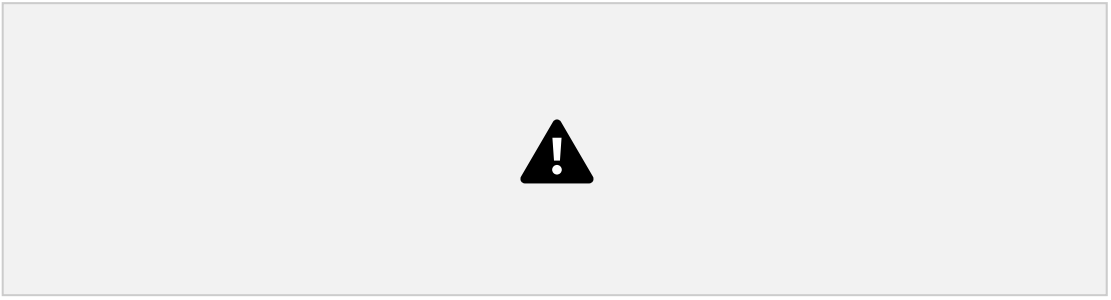

Figure 3.25: J-inverter transform for the WPT system

process, the first step involved the identification of *L* and *M* using formulas as in subsection 3.1.2. Secondly, the key parameters of the *J*-inverter transform, i.e. L_m, J_m, L_R, and J_s, were determined for 405 MHz operating frequency, using the below equations [11, 12]: ◆◆◆◆ , (10)

◆◆ =1

◆◆ ; (9) ◆◆ =◆◆2−◆◆2

2π◆◆◆◆◆◆◆◆

◆◆◆◆◆◆◆◆ =◆◆◆◆

◆◆ =◆◆2−◆◆2

◆◆ ; (11) - (12) ◆◆0

Then the identification of the capacitances, i.e. C_R, C_s, C_{se}, was possible with the help of the provided Eqs. (13)-(15) [11, 12]:

◆◆ =1

◆◆ ; (13) 2π◆◆◆◆◆◆◆◆

◆◆◆◆ =◆◆◆◆

◆◆ - (15) 1+(2π◆◆◆◆◆◆◆◆)2

◆◆ =◆◆◆◆

◆◆ ; (14) 2π◆◆◆◆1−(◆◆◆◆◆◆◆◆0)2

After the calculation of the necessary parameters, the value of the external element C_p was defined as $C_p = C_R C_{se} -$, equaling 3 pF. It is pertinent to highlight that the value of the feeding line length was estimated with the help of Eq. (6) provided in subsection 3.1.2 and determined to be 20.5 mm. Subsequently, the required modification was conducted for good impedance matching, and an updated resonator design was employed in the WPT system establishment, working at a transmission distance of 50 mm.

3.4.3 DNG Metamaterial Modeling

Figure 3.26: DNG MTM design

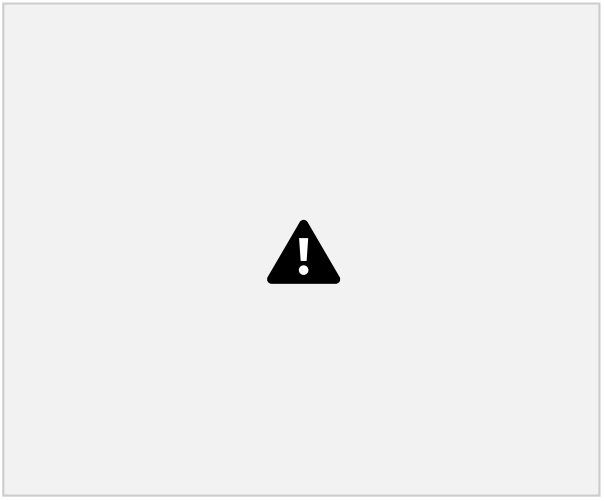

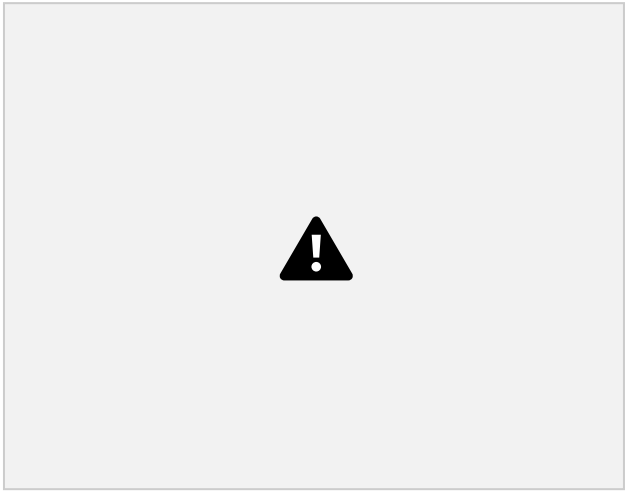

Figure 3.27: Simulation results of MTM slab

This subsection thoroughly examines the realization of DNG MTM, focusing on its design processes. It is imperative to emphasize that this particular MTM structure employs only a single unit cell, allowing miniaturization while maintaining the DNG characteristics at the frequency of interest. Furthermore, the SRR structure was applied in the design, depicted in Fig. 3.26. The square-shaped rings were engineered in a way to show the DNG properties around 405 MHz. Thus, the presented 3 square type rings have 0.3 mm width and 0.3 mm spacing between each other. Fig. 3.27 shows the obtained results of the designed MTM slab, which clearly defines negative values of μ and ε at the necessary range, making it suitable for improvement strategy.

3.4.4 Discussion of Experimental Measurements and Results

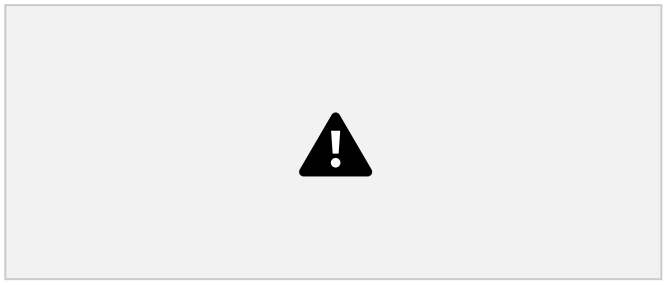

(a) (b)

Figure 3.28: Fabricated prototypes of (a) DGS-based resonator and (b) MTM slab

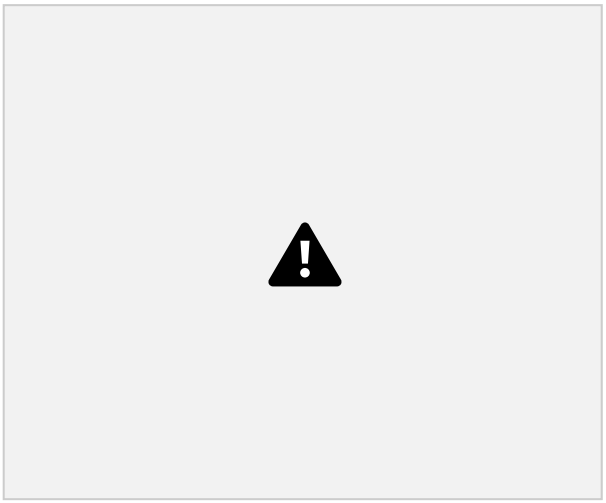

(a) Simulation (b) Experimental

Figure 3.29: Obtained results of the designed WPT system

Fig. 3.28 showcases the manufactured prototypes of the designed DGS-based resonator and DNG MTM. In the simulation and experimental process, the Tx and Rx were placed apart by 50 mm, with the MTM positioned between them in the middle to optimize the performance. According to the EM results from Fig. 3.29a, S_{21} of the WPT system reaches −3.61 dB, which is related to the PTE of 43%. On the other hand, the MTM integration into the designed system results in S_{21} = −1.82 dB, corresponding to 66%. Therefore, the simulation results assert the usefulness of MTM in PTE enhancement. Concerning the experimental results demonstrated in

(a) DGS-based WPT (b) DGS-based WPT with MTM

Figure 3.30: Generated H-field in two scenarios

Fig. 3.29b, the S_{11} value for both cases exceeds −10 dB, indicating the optimal impedance matching. Meanwhile, the S_{21} value equals −6.6 dB for WPT and −2.2 dB for the WPT with integrated MTM slab. This in turn equals PTE of 21.5% and 60%, respectively. The variation between the EM and measured results can be explained by the existence of factors like the impact of in-house manufacturing, losses due to the lumped elements, and the contribution of environmental conditions. Overall, based on the obtained results, it is evident that the MTM addition resulted in the improvement of the DGS-based WPT system. Particularly, the enhancement presented in the PTE rise of up to 38.5%. In addition, Fig. 3.30 validates the usefulness of MTM by showing the enlargement of the H-field with integration, which in turn is related to PTE increase. Consequently, it is safe to claim that the realized DGS-based WPT system with incorporated DNG MTM has the potential to be practically utilized in various applications, including the biomedical field.

3.5 Realization of the Wireless Information and Power Transfer System with DNG Metamaterial Integration

Wireless Information and Power Transfer (WIPT) systems have recently been the subject of interest in research and industry sectors. With the expansion of the application range, the importance of WIPT systems study and development is also growing fast. The areas such as

consumer electronics, RFID, biomedical implants, and IoT sensors, can be considerably enhanced by introducing the capability of transmitting electric energy and data at the same time.

Thereby, this work intended to develop a miniature DGS-based WIPT system, demonstrating dual-band functionality and great performance with DNG MTM addition. In this work, the resonant frequencies were chosen to be 405 MHz and 900 MHz, included in ISM. Furthermore, the DNG MTM was developed using one unit cell to keep the compactness of the full system. Finally, the WPT with integrated MTM was established using dual-band resonators, one serving as Tx and the other as Rx, and MTM positioned in the middle.

3.5.1 Resonator Design

As it was previously mentioned, the resonator is the main building element of the WIPT system. Thus, it is extremely important to design the DGS-based resonator operating at the ISM bands initially. To attain the objective of an efficient system, a strategic decision was made to develop a dual-band system capable of simultaneously transmitting energy and information by applying the cascading approach. This method involves connecting several resonators in a way so they can be excited from one port. Therefore, the two resonators operating at different frequencies are designed at first.

Fig. 3.31a illustrates the proposed DGS-based resonator #1 with a 25-by-12.5 mm^2 area. The composition of the proposed resonating structure is similar to the previous works with RO4350B substrate. It is imperative to note that the defect shape influences the current surface distribution and in turn the resonance occurrence. Hence, the etched slot parameters were determined as x_1 = 7.42 mm, o_1 = 3 mm, while the Eg_1 was defined with a width of 1 mm and

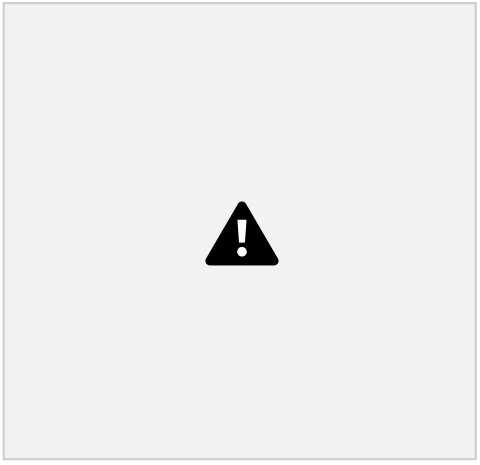

(a) Design (b) Simulation results

Figure 3.31: The proposed resonator at 900 MHz (#1)

length of 3.53 mm. Also, the ML depicted on the top side has w_1 = 3.4 mm and l_1 = 12.5 mm. In

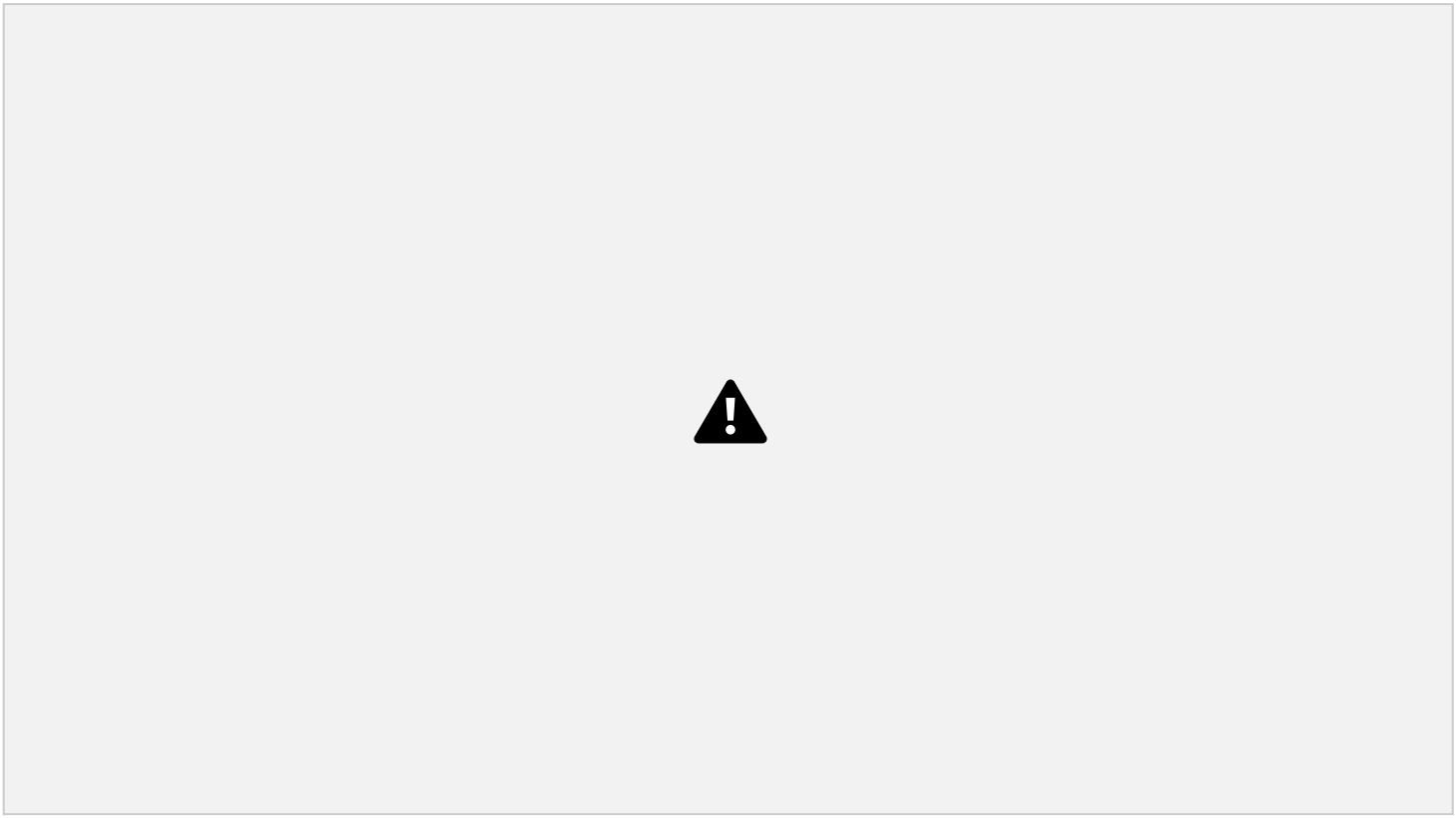

addition, the *parallel LC* represents the EC of the resonator based on DGS as in the earlier structures. The presented design shows the resonance at 3.9 GHz, L = 9.35 nH, and C = 0.6 pF. For operation at 900 MHz, C_{el} with a 2.75 pF value is placed at the Eg_1, as shown in Fig. 3.31b. After, the focus shifts to the resonator #2 design, working at 405 MHz.

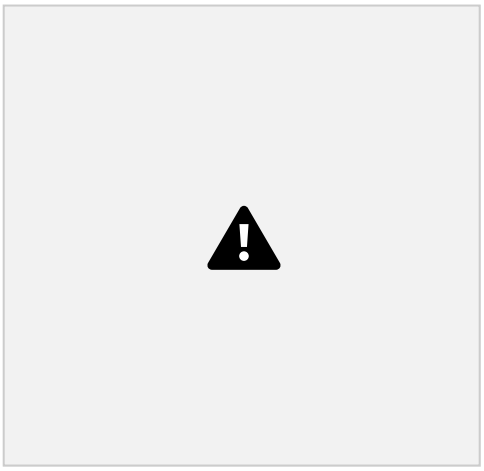

(a) Design (b) Simulation results

Figure 3.32:(a) Design and (b) simulation results of the proposed resonator at 405 MHz (#2)

Fig. 3.32a illustrates the DGS-based resonator with the same size as the #1 structure, working at 405 MHz. The distinguishing feature of this design lies in the defect size, particularly

Figure 3.33: The designed dual-band resonator

Figure 3.34: EM and EC results of the proposed dual-band resonator

the shape of the etched slot is enlarged. Furthermore, the provided EM results in Fig. 3.32b present the 2.51 GHz resonant frequency, corresponding to L = 15.96 nH, and C = 0.18 pF. For

reaching the 405 MHz, the C_{e2} of 9.5 pF is added to the resonator. The final stage in the design of the resonator involves the union of the two developed resonators into one that would be further utilized in the WIPT system establishment.

The final dual-band DGS-based resonator with 25-by-25 sq. mm size is demonstrated in Fig. 3.33 and its EM result is given in Fig. 3.34. It is imperative to note that the modification in external elements was required, which led to C_{e1} = 2.82 pF and C_{e2} = 10.2 pF. Apart from the EM, the EC results were provided to validate the dual-band system's operation. The perfect agreement between them leads to the final resonator usage in the WPT implementation stage.

3.5.2 Dual-Band WIPT System Development

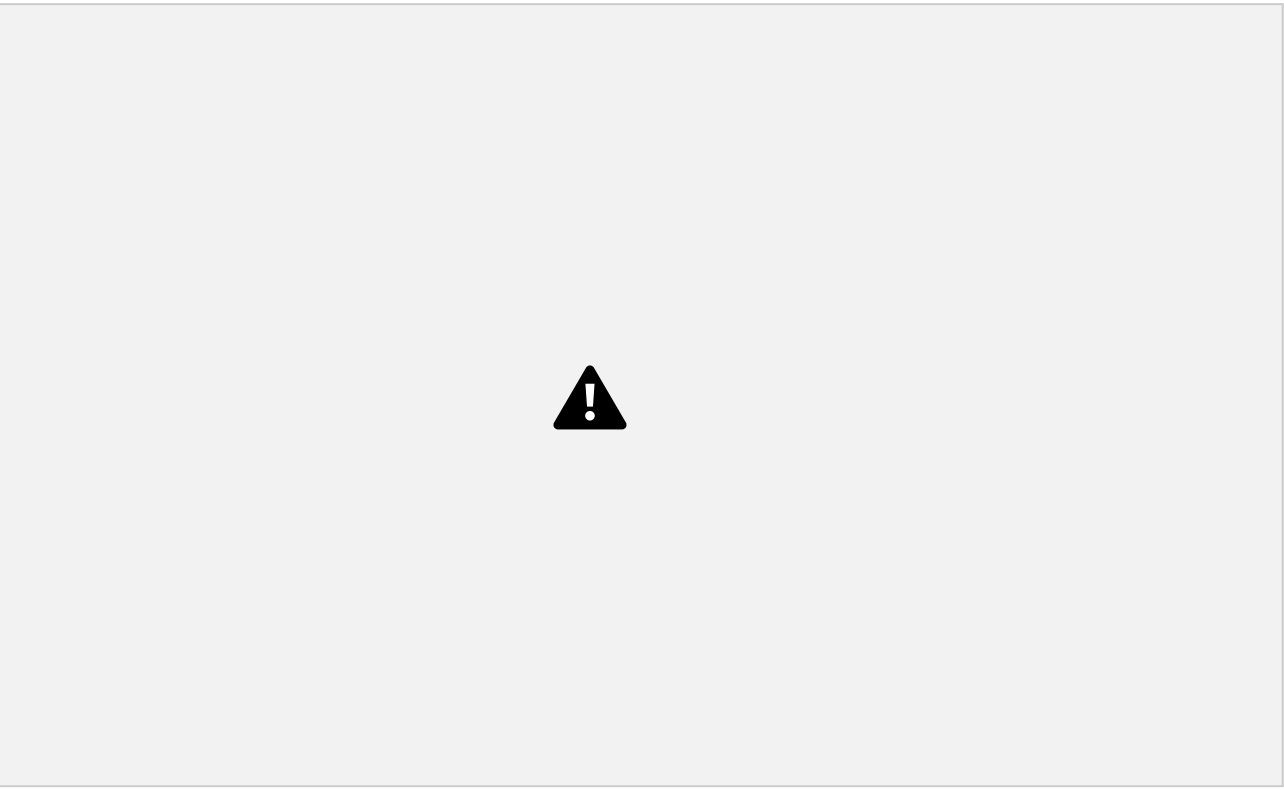

Figure 3.35: The dual-band WIPT system in the simulation domain

Figure 3.36: EM and EC results of the dual-band WIPT system

The WIPT system is established using two identical DGS-based resonators positioned 20 mm apart, as presented in Fig. 3.35. It is essential to mention that achieving impedance matching is required, as the maximum performance can be realized under this condition. Thus, the ML length and external capacitors are commonly optimized for two defects. It is imperative to highlight that using the *J*-inverter technique, it was possible to calculate the stated parameters: 2.35 pF for 900 MHz and 9 pF for 405 MHz. Furthermore, the simulation results are given in Fig. 3.36, which demonstrates the resonance occurrences at 900 MHz and 405 MHz. Concerning the S_{11} values for both frequencies, it is below −10 dB which means the perfect impedance match. Moreover, the good agreement between EM and EC results is also possible to detect.

3.5.3 Realization of DNG Metamaterial

(a) #1 (b) #2

Figure 3.37: Unit cell design

(a) #1 (b) #2

Figure 3.38: Simulation results of the unit cell

In this subsection, the development of a unit cell, possessing the DNG characteristics around two frequencies, is elaborated in detail. It is worth noting that the material composition, as well as area, is identical to the final DGS-based resonator from the former subsection. Initially, unit cell #1 was designed in a manner to exhibit $-\mu$ and $-\varepsilon$ around 900 MHz. Fig. 3.37a shows the proposed design, having a single coil at the top and metallic wire at the bottom. By adjusting the coil parameter, it was possible to meet the stated aim. In detail, the coil width and outer radius of the square were set to 0.3 mm and 11.8 mm, respectively. Fig. 3.38a illustrates the simulated results of unit cell #1, indicating the DNG characteristics at 900 MHz.

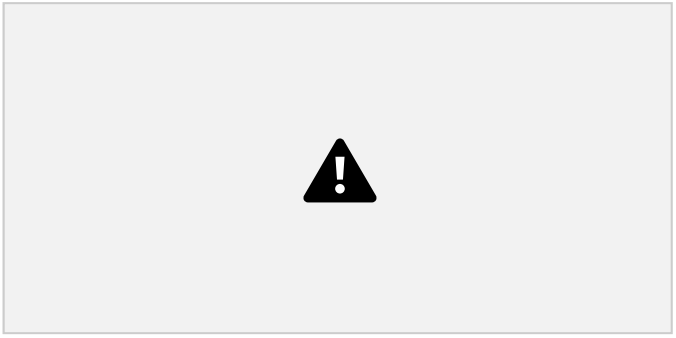

(a) Design

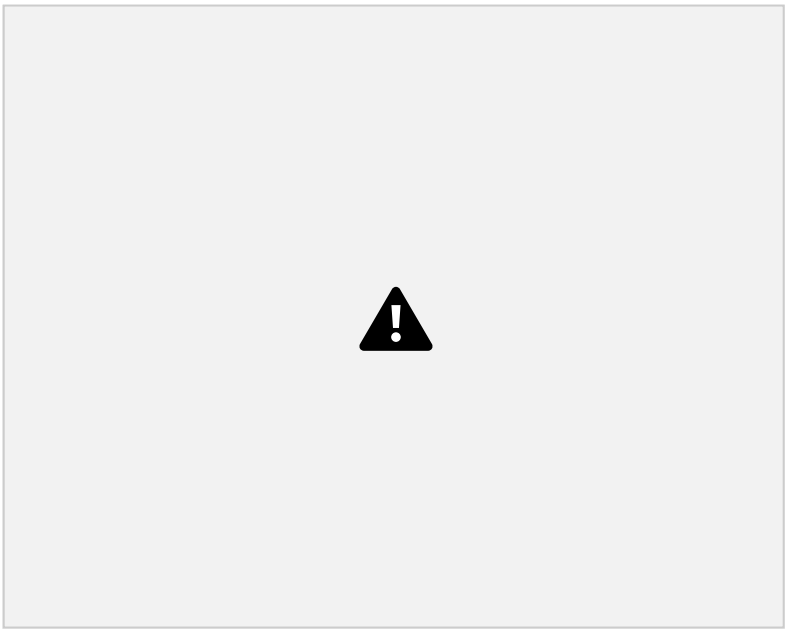

(b) Simulated results

Figure 3.39: Final unit cell

Thus, the focus lay on the design of unit cell #2 having DNG properties around 405 MHz. To reach the mentioned objectives, the coil parameters were adjusted in a way that the coil width (*m*) is 0.3 mm, the spacing between them (*n*) is 0.45 mm, and the outer radius is 10 mm (Fig. 3.37b). Furthermore, the designed unit cell #2 was simulated and resulted in the DNG features at 405 MHz, as depicted in Fig. 3.38b. Finally, the realized unit cells #1 and #2 were combined and presented the DNG characteristics as desired (Fig. 3.39).

3.5.4 Measurement Procedure and

Experimental Results

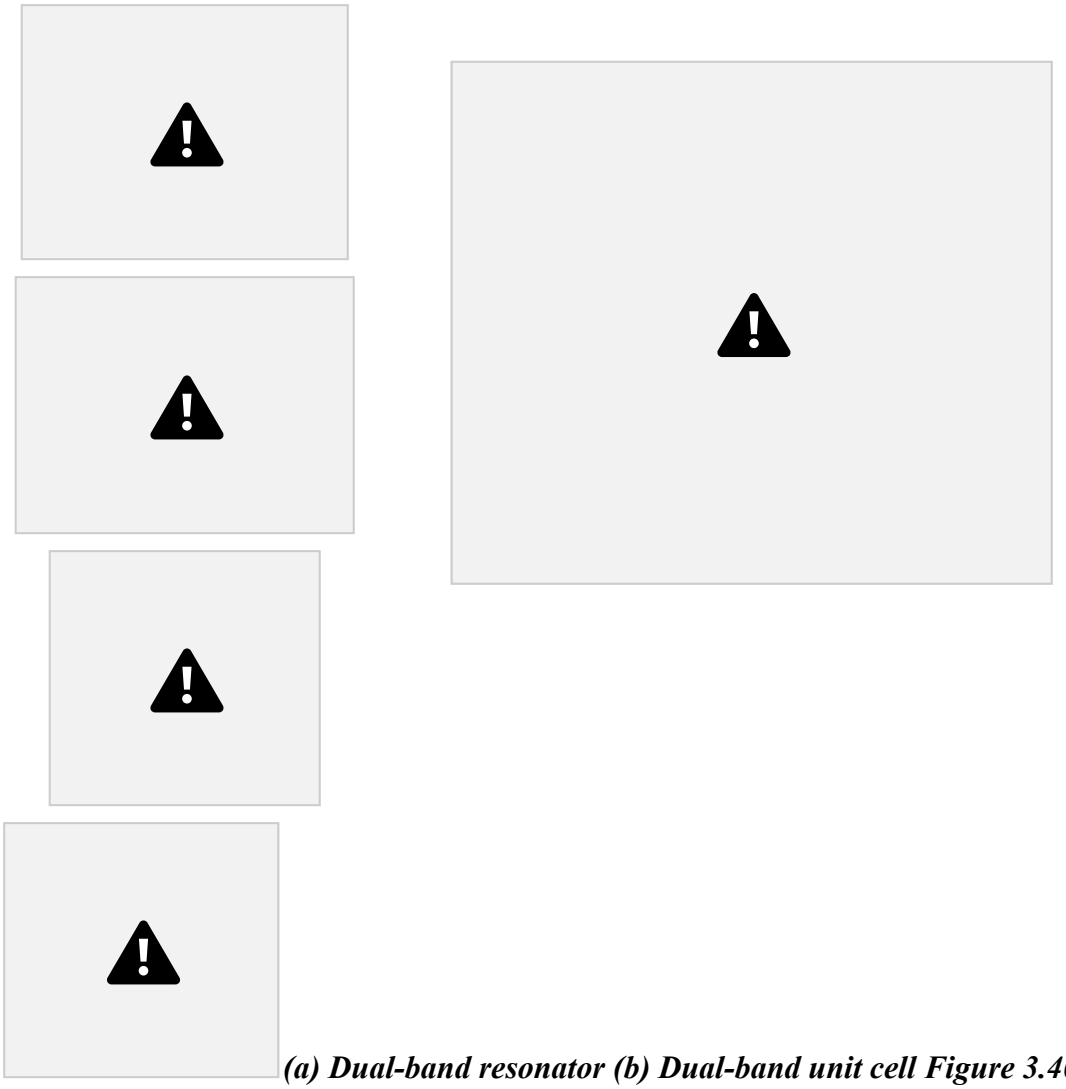

(a) Dual-band resonator (b) Dual-band unit cell Figure 3.40: Manufactured prototypes

(a) WIPT (b) WIPT with DNG MTM

Figure 3.41: Experimental setup

This subsection delves into the measurement setup and result of the dual-band WIPT system with and without DNG MTM integration. Fig. 3.40 showcases the fabricated prototypes of the designed structures. Furthermore, the two resonators were separated by the transfer range of 20 mm. Besides, the experimental validation was performed in two scenarios. The first one

involved the measurement of a dual-band DGS-based WIPT system only, while the second entailed the incorporation of DNG MTM in the middle of the system (Fig. 3.41). Based on the results given in Fig. 3.42, the necessary S_{11} value of -10 dB is obtained in both cases for two frequencies. In terms of PTE, the first case is accompanied by 56% at 405 MHz and 36% at 900 MHz. On the other hand, the second scenario, composed of artificial structure, is associated with the PTE of 71% and 43% at 405 MHz and 900 MHz, accordingly. Considering the obtained outcomes, the improvement of PTE as the result of dual-band DNG MTM addition reached the

Figure 3.42: Experimental results of the WIPT system with and without DNG MTM

values of 14% for 405 MHz and 7% for 900 MHz. Subsequently, the developed WIPT system with integrated MTM slab, functioning at two distinct frequencies, has a great perspective for employment across diverse applications due to the highest compactness and demonstrated superior performance.

Chapter 4 - Conclusions

WPT holds considerable promise as a versatile solution for different applications, aiming

to eliminate the limitations posed by conventional power wires. However, there is still an urgent need for the WPT advancement to overcome well-known problems before becoming an innovative technology. This thesis work achieved certain objectives, directed to enhance the state-of-the-art in the WPT field. In detail, the WPT systems aimed at diverse applications were realized using the MRC technique and DGS-based resonators, spanning various study cases. Particularly, the performed studies and associated achievements are presented as follows:

1) In the first case, the DGS-based WPT system was developed tailored to the biomedical sector, operating at 405 MHz. For this specific application, the size was paramount, leading to the design of the compact system. Afterward, the biological tissue impact was studied and evaluated by introducing the 10 mm chicken breast between the two resonators. This was done to consider a more realistic scenario of WPT system utilization in the implants. Furthermore, the completed SAR analysis confirmed the designed system's potential in the biomedical area.
2) The second implementation of a WPT system was based on the usage of a flexible substrate. During the powering of biomedical implants, there is a high possibility of the Tx side undergoing bending over certain human parts. Consequently, the bending effect on the system performance was studied to ascertain whether it has positive or negative effects. Based on the research results, the bending of the Tx resonator presented the PTE drop by 6%, indicating performance deterioration.
3) In many existing cases, the WPT system measurement results demonstrated poor PTE. This reduction issue is caused by several factors, some of which are unavoidable.

Considering these, the focus of the third research centered on the WPT technology operation advancement, which was based on the employment of MTM slabs of different array configurations. Particularly, MTMs of 2×2 and 3×3 arrangements, exhibiting negative permeability, were integrated into the system. According to the results, the

realized WPT with 3×3 MTM incorporation reached the peak PTE enhancement of 11%.

4) Many designed MTM slabs added into the WPT system possessed bulky dimensions, causing limitations to the utilization applications. Thus, the fourth investigation concentrated on the development of the compact MTM structure, possessing double negative properties. The addition of designedMTM, having the size of the resonator, into the WPT system resulted in a 38.5% PTE rise.

5) The last research involved the WIPT system implementation, functioning at two different ISM frequencies. It is important to note that the dual-band functionality allows power and data transmission simultaneously, extending the applicability of the developed system. In addition, the compact MTM, exhibiting double negative characteristics at two bands, was also designed and employed for performance improvement. Finally, the established WIPT system with integrated MTM demonstrated supreme performance.

Overall, the completed research comprehensively examines the design and realization of the WPT, with particular attention on maintaining the miniature structure while improving the PTE. Moreover, the conducted study also delves into the development and employment of miniature MTM slabs for the purpose of performance enhancement. As a result, the verification of MTM slabs' usefulness in efficiency increase was aptly demonstrated. It is pertinent to note that the validity of the constructed designs was efficiently and practically checked in the real environment with all prototyping completed. It is safe to conclude that the performed work

contributes to the advancement of the state-of-the-art in WPT technology and gives perspectives for future innovations in this developing field. Hence, the following aspects can be examined in future research works:

1) The misalignment of the resonators can drastically deteriorate the WPT performance, particularly leading to the PTE drop and shift of the resonance occurrence. Therefore, it is

crucial to consider the stated issue in the future study to achieve a more robust WPT.

2) The external material in between the coupled resonators has a significant impact on the system PTE. Thus, it is highly recommended to consider different materials in future works to realize a reliable and stable system that has protection against material exposure.

3) In most known cases, the DGS-based WPT systems present superior performance but in the short transfer ranges. Subsequently, there is a need for future studies, aimed at distance increase strategies, ensuring the rise of WPT system flexibility.

4) Technologies that permit the charging of several devices simultaneously have received great interest and recognition recently. Thus, future investigations may involve the WPT systems implementation of different input and output configurations for increasing overall efficiency and suitability to various fields.

Bibliography

[1] K. Dautov *et al.*, "Compact multi-frequency system design for SWIPT applications," *International Journal of RF and Microwave Computer-Aided Engineering*, vol. 31, no. 6, 2021, Art. no. e22632.

[2] H. A. Atallah, "Design of compact high efficient WPT system utilizing half ring resonators (HRRs) DGS for short range applications," *35th National Radio Science Conference (NRSC)*, Cairo, Egypt, 2018, pp. 63-68.

[3] S. Malhotra, S. Verma, V. Bohara, and M. Hashmi, "Dual-band WPT system using Semi-H DGS for Biomedical Applications," *IEEE Asia-Pacific Microwave*

Conference (APMC), Singapore, 2019, pp. 720-722.

[4] A. Banerji *et al.*, "Wireless transfer of power: Status and challenges," *International Conference on Intelligent Control Power and Instrumentation (ICICPI)*, Kolkata, India, 2016, pp. 251-257.

[5] D. Kim, A. Abu-Siada, and A. Sutinjo, "State-of-the-art literature review of WPT: Current limitations and solutions on IPT," *Electric Power Systems Research*, vol. 154, pp. 493–502, Jan. 2018.

[6] S. Malhotra and M. Hashmi, "Near-Field WPT using Defected Ground Structures for UHF RFID Applications," *IEEE International Conference on RFID Technology and Applications (RFID-TA)*, Pisa, Italy, 2019, pp. 16-21.

[7] X. Gu, S. Hemour, and K. Wu, "Far-Field Wireless Power Harvesting: Nonlinear Modeling, Rectenna Design, and Emerging Applications," *Proceedings of the IEEE*, vol. 110, no. 1, pp. 56-73, Jan. 2022.

[8] S. Maoqiang *et al.*, "Study of Metamaterial on Efficiency of DGS-based MISO-WPT system," *Wireless Power Week (WPW)*, Bordeaux, France, 2022, pp. 344-348.

[9] Y. D. Lee, K. W. Kim, and G. W. Moon, "A Self-Compensated Planar Coil With Integrated Single-Switch Regulator for Wireless Power Transfer (WPT) Systems," *IEEE Transactions on Power Electronics*, vol. 36, no. 10, pp. 10954-10958, Oct. 2021.

[10] M. S. Yusri *et al.*, "Transfer Efficiency Enhancement on Wireless Power Transfer Using Metamaterial," *International Conference on Information Technology (ICIT),* Amman, Jordan, 2023, pp. 724-729.

[11] F. Tahar *et al.*, "Dual-Band Defected Ground Structures Wireless Power Transfer System With Independent External and Inter-Resonator Coupling," *IEEE Transactions on Circuits and Systems II: Express Briefs*, vol. 64, no. 12, pp. 1372-1376, Dec. 2017.

[12] N. Mohamed *et al.*, "A Comprehensive Analysis of Wireless Charging Systems for Electric Vehicles," *IEEE Access*, vol. 10, pp. 43865-43881, 2022.

[13] M. Aboualalaa and R. K. Pokharel, "Reliable Multiple Cascaded Resonators WPT System Using Stacked Split-Ring Metamaterial Passive Relays," *IEEE Transactions on Instrumentation and Measurement*, vol. 72, pp. 1-10, 2023, Art no. 8006710.

[14] F. Ferreira *et al*., "Compact Near Field Wireless Energy Transfer Systems Using Defected Ground Structures," *IEEE Journal of Microwaves*, vol. 3, no. 3, pp. 951-961, July 2023.

[15] K. Dautov, M. Hashmi, G. Nauryzbayev, and N. Nasimuddin, "Recent Advancements in Defected Ground Structure-Based Near-Field Wireless Power Transfer Systems," *IEEE Access*, vol. 8, pp. 81298-81309, 2020.

[16] D. Kupreyev, K. Dautov, M. Hashmi, and M. A. Chaudhary, "High-Performance Planar

Hexagonal Coil-Type Wireless Power Transfer System," *IEEE MTT-S Latin America Microwave Conference (LAMC 2020)*, Cali, Colombia, 2021, pp. 1-3.

[17] W. Lee and Y. K. Yoon, "High Efficiency Metamaterial-based Multi-scale Wireless Power Transfer for Smart Home Applications," *2021 IEEE MTT-S International Microwave Symposium (IMS)*, Atlanta, GA, USA, 2021, pp. 62-65.

[18] S. Verma, D. Rano, and M. Hashmi, "A Novel Dual Band Defected Ground Structure for Short Range Wireless Power Transfer Applications," *IEEE Wireless Power Transfer Conference (WPTC)*, London, UK, 2019, pp. 188-191.

[19] A. Bhattacharya, T. Shaw, and D. Mitra, "Performance Enhancement of Wireless Power Transfer System by Controlling Transmission and Reflection Properties of Metamaterials," *IEEE MTT-S International Microwave and RF Conference (IMaRC)*, Kolkata, India, 2018, pp. 1-4.

[20] S. Alshhawy, A. Barakat, K. Yoshitomi, and R. K. Pokharel, "Compact and Efficient WPT System to Embedded Receiver in Biological Tissues Using Cooperative DGS Resonators," *IEEE Transactions on Circuits and Systems II: Express Briefs*, vol. 69, no. 3, pp. 869-873, March 2022.

[21] Q. Wang, W. Che, M. Mongiardo, and G. Monti, "Wireless Power Transfer System With High Misalignment Tolerance for Bio-Medical Implants," *IEEE Transactions on Circuits and Systems II: Express Briefs*, vol. 67, no. 12, pp. 3023-3027, Dec. 2020.

[22] A. Barakat, K. Yoshitomi, and R. K. Pokharel, "Design Approach for Efficient Wireless Power Transfer Systems During Lateral Misalignment," *IEEE Transactions on Microwave Theory and Techniques*, vol. 66, no. 9, pp. 4170-4177, Sept. 2018.

[23] Y. Li *et al*., "Maximizing Transfer Distance for WPT via Coupled Magnetic Resonances by Coupling Coils Design and Optimization," *IEEE Access*, vol. 8, pp. 74157-74166, 2020.

[24] X. Jiang *et al*., "Efficient and Compact Dual-band Wireless Power Transfer System through Biological Tissues Using Dual-Reference DGS Resonators," *IEEE MTT-S International Microwave Symposium (IMS)*, Atlanta, GA, USA, 2021, pp. 54-57.

[25] M. Heshmatzadeh, A. A. Lotfi-Neyestanak, and S. Noghanian, "Improving Wireless Power Transfer Efficiency Using Fractal Metamaterial for Wearable Applications," *2023 IEEE International Symposium on Antennas and Propagation and USNC-URSI Radio Science Meeting (USNC-URSI)*, Portland, OR, USA, 2023, pp. 535-536.

[26] T. Shaw and D. Mitra, "Wireless Power Transfer System Based on Magnetic Dipole Coupling With High Permittivity Metamaterials," *IEEE Antennas and Wireless Propagation Letters*, vol. 18, no. 9, pp. 1823-1827, Sept. 2019.

[27] C. Lecluyse, B. Minnaert, and M. Kleemann, "A Review of the Current State of

Technology of Capacitive Wireless Power Transfer," *Energies*, vol. 14, no. 18, p. 5862, Sep. 2021.

[28] W. Lin and R. W. Ziolkowski, "Far field wireless power transfer for IoT applications enabled by an ultra-compact and highly-efficient Huygens rectenna," *IEEE Wireless Power Transfer Conference (WPTC)*, Seoul, Korea (South), 2020, pp. 69-71.

[29] A. K. Baghel, S. S. Kulkarni, and S. K. Nayak, "Far-Field Wireless Power Transfer Using GRIN Lens Metamaterial at GHz Frequency," *IEEE Microwave and Wireless Components Letters*, vol. 29, no. 6, pp. 424-426, June 2019.

[30] Z. Popovic, "Far-field wireless power delivery and power management for low-power sensors," *IEEE Wireless Power Transfer (WPT)*, Perugia, Italy, 2013, pp. 1-4.

[31] M. Aboualalaa *et al.*, "Improvement of Magnetic Field for Near-Field WPT System Using Two Concentric Open-Loop Spiral Resonators," *IEEE Microwave and Wireless Components Letters*, vol. 30, no. 10, pp. 993-996, Oct. 2020.

[32] T. Mehta, S. Dey, and S. Dey, "Near-Field Inductive Wireless Power Transfer at ISM Bands for Biomedical Applications," *IEEE Microwaves, Antennas, and Propagation Conference (MAPCON)*, Bangalore, India, 2022, pp. 1439-1443.

[33] W. Zhou *et al.*, "Potential and Challenges of Capacitive Power Transfer Systems for Wireless EV Charging: A Re-view of Key Technologies," *Green Energy and Intelligent Transportation*, pp. 100174–100174, Jan. 2024.

[34] G. Wei *et al.*, "An Automatic Coil Design Method With Modified AC Resistance Evaluation for Achieving Maximum Coil–Coil Efficiency in WPT Systems," *IEEE Transactions on Power Electronics*, vol. 35, no. 6, pp. 6114-6126, June 2020.

[35] I. S. Jeong, B. I. Jung, D. S. You, and H. S. Choi, "Analysis of S-Parameters in Magnetic Resonance WPT Using Superconducting Coils," *IEEE Transactions on Applied Superconductivity*, vol. 26, no. 3, pp. 1-4, April 2016, Art no. 0501004.

[36] Z. Yin, S. Yu, and N. Kou, "Robust Wireless Power Transfer System Using Gain Element as Source for Conformal Application," *IEEE Microwave and Wireless Technology Letters*, vol. 34, no. 1, pp. 127-130, Jan. 2024.

[37] S. Verma, D. Rano, and M. S. Hashmi, "Enhancing the performance of defected ground structure type near‐field radiofrequency WPT system by coupled‐line impedance matching," *Iet Microwaves Antennas & Propagation*, vol. 14, no. 12, pp. 1431–1439, Jul. 2020.

[38] J. Chen and H. Tan, "Metamaterial for wireless power transfer system at 13.56MHz with coil misalignment," *7th IEEE International Symposium on Microwave, Antenna, Propagation, and EMC Technologies (MAPE)*, Xi'an, China, 2017, pp. 313-317.

[39] C. Rong *et al.*, "Analysis of wireless power transfer based on metamaterial using equivalent circuit," *The Journal of Engineering*, vol. 2019, no. 16, pp. 2032–2035, Dec. 2018.

[40] A. Iqbal *et al.*, "Wireless power transfer system for deep-implanted biomedical devices," *Scientific Reports*, vol. 12, no. 1, Aug. 2022.

[41] P. Feng *et al*., "Chip-Scale Coils for Millimeter-Sized Bio-Implants," *IEEE Transactions on Biomedical Circuits and Systems*, vol. 12, no. 5, pp. 1088-1099, Oct. 2018.

[42] A. Basir and H. Yoo, "Efficient Wireless Power Transfer System With a Miniaturized Quad-Band Implantable Antenna for Deep-Body Multitasking Implants," *IEEE Transactions on Microwave Theory and Techniques*, vol. 68, no. 5, pp. 1943-1953, May 2020.